

1 Passive source reverse time migration based on the 2 spectral element method

3 Bin He¹, Yu Chen¹, David Lumley^{1,2}, Qinya Liu^{3,4}, Nozomu Takeuchi⁵, Hitoshi
4 Kawakatsu⁵, and Hejun Zhu^{1,2}

5 ¹Department of Geosciences, The University of Texas at Dallas, Richardson, TX 75080, USA

6 ²Department of Physics, The University of Texas at Dallas, Richardson, TX 75080, USA

7 ³Department of Physics, University of Toronto, Toronto M5S 1A7, Canada

8 ⁴Department of Earth Sciences, University of Toronto, Toronto M5S 3B1, Canada

9 ⁵Earthquake Research Institute, University of Tokyo, Tokyo 1130032, Japan

10 Key Points:

- 11 • A 3-D passive source reverse time migration based on the spectral element method
12 is proposed to image complex structures.
- 13 • Amplitude-preserved vector P and S wavefields are accurately decomposed by solv-
14 ing corresponding weak-form solutions.
- 15 • Several south-dipping structures can be identified from P and S migration results
16 beneath the Laramie basin, which are interpreted as the Cheyenne Belt suture zone.

17 **Abstract**

18 Increasing deployment of dense arrays has facilitated detailed structure imaging
19 for tectonic investigation, hazard assessment and resource exploration. Strong velocity
20 heterogeneity and topographic changes have to be considered during passive source imag-
21 ing. However, it is quite challenging for ray-based methods, such as Kirchhoff migration
22 or the widely used teleseismic receiver function, to handle these problems. In this study,
23 we propose a 3-D passive source reverse time migration strategy based on the spectral
24 element method. It is realized by decomposing the time reversal full elastic wavefield into
25 amplitude-preserved vector P and S wavefields by solving the corresponding weak-form
26 solutions, followed by a dot-product imaging condition to get images for the subsurface
27 structures. It enables us to use regional 3-D migration velocity models and take topo-
28 graphic variations into account, helping us to locate reflectors at more accurate positions
29 than traditional 1-D model-based methods, like teleseismic receiver functions. Two syn-
30 synthetic tests are used to demonstrate the advantages of the proposed method to handle
31 topographic variations and complex velocity heterogeneities. Furthermore, applications
32 to the Laramie array data using both teleseismic P and S waves enable us to identify sev-
33 eral south-dipping structures beneath the Laramie basin in southeast Wyoming, which
34 are interpreted as the Cheyenne Belt suture zone and agree with, and improve upon pre-
35 vious geological interpretations.

36 **Plain Language Summary**

37 Increasing deployment of dense arrays has allowed detailed structure imaging for
38 tectonic investigation, hazard assessment and resource exploration. However, traditional
39 ray-based migration methods or 1-D velocity model-based receiver function methods may
40 greatly degrade the imaging quality without considering the full wavefield propagation
41 effect and velocity heterogeneities. Therefore, in this study, we develop a 3-D passive source
42 migration based on the spectral element method, which is capable of handling topographic
43 variations as well as complex velocity heterogeneities for real data applications. Several
44 synthetic tests and applications to the Laramie array data using both teleseismic P and
45 S waves are used to demonstrate the capability of our method to image complex struc-
46 tures, such as subduction and suture zones.

47 1 Introduction

48 In past decades, teleseismic receiver functions have been widely used for imaging
49 discontinuities within the Earth's crust and upper mantle (Burdick & Langston, 1977;
50 Langston & Corvallis, 1977; Vinnik, 1977; Ai et al., 2007; Kawakatsu & Watada, 2007;
51 Kind et al., 2012; H. Zhang et al., 2016; Long et al., 2019). Based on the assumption of
52 a 1-D Earth model where discontinuities are horizontal, common convert point stack-
53 ing (Dueker & Sheehan, 1997; L. Zhu, 2000; Gilbert et al., 2003) has generally been used
54 to improve the image quality by mapping the receiver functions to depths. In the case
55 of a single station, like the SEIS on Mars (Banerdt et al., 2020; Knapmeyer-Endrun et
56 al., 2020; Lognonné et al., 2020) or sparse station distributions such as the USArray (Meltzer
57 et al., 1999), such simplifications are natural and useful. However, it indeed degrades the
58 image quality of geologically complex structures, such as subsurface environments with
59 steep faults and laterally discontinuous interfaces, without considering the effects of wave-
60 field diffraction and scattering caused by lateral variations of impedance contracts and
61 velocities (L. Chen et al., 2005; Shang et al., 2012). In addition, increasing deployment
62 of dense and nodal arrays has facilitated detailed structure imaging for tectonic inves-
63 tigation, hazard assessment and resource exploration (Okada et al., 2004; Zheng et al.,
64 2008; Nábělek et al., 2009; H. Zhang et al., 2016; X. Yang et al., 2017; X. Chen et al.,
65 2018; Li et al., 2018; Clayton et al., 2019; X. Wang et al., 2021; Onyango et al., 2022;
66 Wu et al., 2023). Therefore, it calls for advanced imaging methods, such as seismic mi-
67 gration/inversion, which exploit the full complexity of recorded wavefields and rely less
68 on a priori information about the Earth's structures, to get accurate images of complex
69 subsurface discontinuities (Sheehan et al., 2000; L. Chen et al., 2005; Shang et al., 2012;
70 Cheng et al., 2016; Li et al., 2018; Millet et al., 2019).

71 Among many seismic migration approaches, Kirchhoff migration/inversion (Schneider,
72 1978; Gray & May, 1994) has been widely used in the oil and gas industry to image shal-
73 low sedimentary structures owing to its high efficiency and simplicity. It was later in-
74 troduced to global seismology for imaging large-scale structures using multi-component
75 teleseismic data recorded by local dense arrays (Burridge et al., 1998; Bostock, 1998; Bo-
76 stock & Rondenay, 1999; Rondenay et al., 2000; Bostock et al., 2001; Bostock, 2002; Levan-
77 der et al., 2005; Rondenay, 2009; Liu & Levander, 2013; Cheng et al., 2016; Millet et al.,
78 2019). Teleseismic Kirchhoff migration/inversion is implemented by weighting and stack-
79 ing data along diffraction hyperbola for every possible scattering point in a regular grid

(Schneider, 1978; Gray & May, 1994; Bostock et al., 2001; Cheng et al., 2016; Millet et al., 2019). To date, most Kirchhoff migration/inversion approaches are based on the infinite high-frequency assumption by neglecting the finite frequency property of seismic wave propagation, which enables us to efficiently get images by using ray tracing (Richards & Aki, 1980) or solving the Eikonal equation (Gray & May, 1994; Cheng et al., 2016). However, It is difficult for ray-tracing to handle multiple arrivals, shadow zones, and even chaotic rays in complex subsurface environments (Audebert et al., 1997; L. Chen et al., 2005). Although the Eikonal equation-based Kirchhoff migration is capable of dealing with complex structures, it is not easy to handle the multipathing challenge (H. Zhao, 2005; Waheed et al., 2015; Tong, 2021). Furthermore, Kirchhoff migration requires more efforts to correct image amplitudes, and therefore, the wave-equation Kirchhoff migration has been developed to balance accuracy and efficiency (Andrade et al., n.d.; Jin & Etgen, n.d.). To mitigate the finite-frequency, multi-arrivals and inaccurate amplitude problems, Gaussian beam migration (Hill, 1990, 2001) has been proposed to apply local slant stacks by using complex-valued traveltimes and amplitudes. These complex quantities come from the approximation of seismic wave propagation with a sum of Gaussian beams, which are finite-frequency, ray-theoretical approximations to the wave equation (Notfors et al., n.d.). It is further extended to the wave-equation-based two-way beam wave method, which has comparable accuracy and efficiency in comparison to the wave-equation-based methods (J. Yang et al., 2022).

On the other hand, wave equation-based migration methods can essentially avoid most difficulties from the ray-based method by using the full wavefields (Claerbout, 1985). Among many different types of wave equation-based migration methods, synthetic and field experiments have shown that reverse-time migration (RTM) (Baysal et al., 1983; Whitmore, 1983; McMechan, 1983) has better performance for imaging complex structures. Active source RTM includes a forward wavefield modeling from the source and a backward wavefield modeling from the receivers, followed by applying imaging conditions to these two wavefields. In contrast, passive source RTM only requires one backward wavefield modeling for each earthquake. Therefore, inaccuracies due to source locations and velocity variations between earthquake locations and local study regions could be neglected. During the wavefield back-propagation, P and S wavefields are usually separated by polarization decomposition (Shang et al., 2012; H. Zhu, 2017; J. Yang et al., 2018). Then, the imaging condition is applied to cross-correlate separated P and S wave-

fields, followed by the summation of individual events. As pointed out by Shang et al. (2012), passive source RTM of converted waves differs fundamentally from single station receiver function analysis, and also in several important ways from more traditional receiver function migration (L. Chen et al., 2005). However, both current 2-D and 3-D pioneer works are based on the finite difference method, which requires projecting station locations on the model grids, and it is not easy to handle complex topography in real applications (Rajasekaran & McMechan, 1995; Bevc, 1997; Shragge, 2014; Shang et al., 2017; Yi et al., 2019). In addition, there are few real data applications for 3-D passive source RTM to image crustal and uppermost mantle structures.

In this study, we combine passive source RTM with the spectral-element method (SEM) (Komatitsch & Vilotte, 1998; Fichtner et al., 2009). Owning to its advantages in handling complex topographic variations, wavefield coupling between different media, flexibility to handle station distributions and so on, the SEM has been widely applied to construct crustal and mantle velocity models at regional and global scales (Tromp et al., 2005; Fichtner et al., 2009; Tape et al., 2009; Fichtner, 2010; Liu & Levander, 2013; H. Zhu et al., 2012; Y. Wang et al., 2016; K. Wang et al., 2020, 2021; Tromp, 2020; H. Zhu et al., 2020; Maguire et al., 2022). Here, we use it for passive source RTM. Because the wave-equation is solved in a weak-form fashion in SEM, directly taking strong-form spatial derivatives for wavefield decomposition results in significant discontinuities between element boundaries. To solve this problem, we propose to solve the corresponding weak-form solutions for P and S wavefield decomposition. This paper is organized into the following parts, we first briefly review passive source RTM based on the wavefield decomposition, followed by the theory of weak-form solutions for wavefield decomposition, and then several synthetic tests are used to demonstrate the advantages of the proposed method. Finally, we apply it to the Laramie array for suture zone imaging.

2 Methodology

2.1 Passive source RTM based on vector wavefield decomposition

Based on the principle that all back-propagating direct P and S receiver wavefields (\mathbf{u}^P and \mathbf{u}^S) should coincide at “source” locations, wave-equation-based passive source imaging seeks strong energy in space as the source locations (McMechan, 1982; Nakata & Beroza, 2016; J. Yang et al., 2020; Duan et al., 2021). Similarly, the vector \mathbf{u}^P and

¹⁴⁴ \mathbf{u}^S wavefields constructed by back-propagating multichannel direct P and Ps converted
¹⁴⁵ (or direct S and Sp converted) seismograms, should coincide at the scattering locations
¹⁴⁶ in depths, such as the Moho (Shang et al., 2012; Li et al., 2018). The imaging condition
¹⁴⁷ can be given as

$$I(\mathbf{x}) = \sum_{i_e=1}^{N_e} \int_{t=0}^T \mathbf{u}(\mathbf{x})_{i_e}^P(t) \cdot \mathbf{u}(\mathbf{x})_{i_e}^S(t) dt , \quad (1)$$

¹⁴⁸ where $I(\mathbf{x})$ is the image, $\mathbf{u}(\mathbf{x})_{i_e}^P$ and $\mathbf{u}(\mathbf{x})_{i_e}^S$ are the constructed vector P and S wavefields
¹⁴⁹ for i_e th event at the spatial coordinate \mathbf{x} . N_e is the total number of events for imaging.
¹⁵⁰ t represents the current time and T denotes the total time for wavefield back-propagation.
¹⁵¹ “ \cdot ” denotes the dot product between two vector fields. The final image is obtained by
¹⁵² summing over all the time steps during wavefield back-propagation and all seismic events.

¹⁵³ Because the vector \mathbf{u}^P and \mathbf{u}^S wavefields are coupled during elastic wavefield sim-
¹⁵⁴ ulations, one may consider back-propagate multichannel P and Ps (or S and Sp) seis-
¹⁵⁵ mograms independently by solving two acoustic wave-equations (Sun et al., 2004; Duan
¹⁵⁶ et al., 2021) or decouple them during the wavefield back-propagation. H. Zhu (2017) pro-
¹⁵⁷ posed an amplitude-preserved wavefield decomposition method to decouple the vector
¹⁵⁸ \mathbf{u}^P and \mathbf{u}^S from elastic wavefield \mathbf{u} by introducing a vector \mathbf{w} in the form of

$$\nabla^2 \mathbf{w} = \mathbf{u} = \mathbf{u}^P + \mathbf{u}^S , \quad (2)$$

¹⁵⁹ where vector P and S wavefields can be obtained according to

$$\mathbf{u}^P = \nabla(\nabla \cdot \mathbf{w}), \quad \mathbf{u}^S = -\nabla \times \nabla \times \mathbf{w} . \quad (3)$$

¹⁶⁰ Here ∇ , $\nabla \cdot$ and $\nabla \times$ are the gradient, divergence and curl operators, respectively. How-
¹⁶¹ ever, solving Equation 3 requires explicitly solving the Poisson's equation in Equation
¹⁶² 2. To reduce the computational costs, J. Yang et al. (2018) further extended this method
¹⁶³ to avoid solving Poisson's equation under the isotropic media assumption with

$$\mathbf{u}^P = \nabla(\nabla \cdot \alpha^2 \hat{\mathbf{u}}), \quad \mathbf{u}^S = -\nabla \times (\nabla \times \beta^2 \hat{\mathbf{u}}) , \quad (4)$$

¹⁶⁴ where $\hat{\mathbf{u}}$ denotes the extrapolated wavefield excited by a double integral of the original
¹⁶⁵ seismograms, α and β are the local P and S velocities, respectively.

¹⁶⁶ 2.2 Strong- and weak-form solutions for the wavefield decomposition

¹⁶⁷ In this section, we introduce H. Zhu (2017) and J. Yang et al. (2018)'s method to
¹⁶⁸ the SEM, so that it is more convenient to handle irregular surface topography and sta-

169 tion locations. Different from the finite difference (FD) method, SEM seeks a weak so-
 170 lution $\bar{\mathbf{u}}(\mathbf{x}, t)$ to the equation of motion in the Galerkin sense (Komatitsch & Vilotte,
 171 1998; Fichtner, 2010). Lagrange polynomials collocated at the Gauss–Lobatto–Legendre(GLL)
 172 points are used to interpolate the wavefield at any spatial locations in the form of

$$\mathbf{u}(\mathbf{x}, t) \approx \bar{\mathbf{u}}(\mathbf{x}, t) = \sum_{i,j,k=1}^{N+1} \mathbf{u}^{ijk}(t) L_{ijk}(\mathbf{x}) , \quad (5)$$

173 where $\mathbf{u}(\mathbf{x}, t)$ and $\bar{\mathbf{u}}(\mathbf{x}, t)$ represent the true and weak-form solutions of the wave-equation,
 174 respectively. \mathbf{x} represents the spatial coordinate and t represents time. N denotes the
 175 degree of the Lagrange polynomials, and therefore we have $N + 1$ GLL points for one
 176 element along each direction. $L_{ijk} = l_i(x)l_j(y)l_k(z)$ represents the basis function cho-
 177 sen as the product of three Lagrange polynomials $l(x)$, $l(y)$ and $l(z)$ along the x, y and
 178 z directions collocated at the corresponding GLL points.

179 Owing to the continuous properties of the Lagrange polynomials, a straightfor-
 180 ward solution of Equation 4 based on SEM, noted as the strong-form solution, can be
 181 realized by

$$\mathbf{u}^P = \nabla[\nabla \cdot \alpha^2 \sum_{i,j,k=1}^{N+1} \mathbf{u}^{ijk}(t) L_{ijk}(\mathbf{x})], \quad \mathbf{u}^S = -\nabla \times [\nabla \times \beta^2 \sum_{i,j,k=1}^{N+1} \mathbf{u}^{ijk}(t) L_{ijk}(\mathbf{x})] , \quad (6)$$

182 which is fairly easy to implement because the spatial derivatives from the gradient, di-
 183 vergence and curl operators are taken from the Lagrange polynomials. However, we ex-
 184 pect quite strong artifacts in the separated vector wavefields, which could contaminate
 185 the final imaging result. As illustrated in Figure 1, strong S mode artifacts appear in the
 186 P mode. This is because the solution of SEM is a weak-form approximation, and although
 187 the wavefield is continuous cross elements, the continuity of spatial derivatives is not guar-
 188 anteed. To mitigate this leakage during wavefield decomposition, we use the weak so-
 189 lutions for Equation 4 as follows:

$$\int_{G_e} \Phi \cdot \mathbf{u}^P d^3\mathbf{x} = \int_{G_e} \Phi \cdot \nabla(\nabla \cdot \alpha^2 \mathbf{u}) d^3\mathbf{x} = - \int_{G_e} [\nabla \cdot \Phi][\nabla \cdot (\alpha^2 \mathbf{u})] , \quad (7)$$

$$\int_{G_e} \Phi \cdot \mathbf{u}^S d^3\mathbf{x} = - \int_{G_e} \Phi \cdot \nabla \times (\nabla \times \beta^2 \mathbf{u}) d^3\mathbf{x} = \int_{G_e} [\nabla \times \Phi] \cdot [\nabla \times \beta^2 \mathbf{u}] d^3\mathbf{x} , \quad (8)$$

190 where Φ denotes any arbitrary, differentiable, time-independent test function, which will
 191 be chosen as the basis functions similar to the way we get SEM solutions. As shown in
 192 Figure 2, both P and S modes are clearly separated without significant leakages. This
 193 indicates that the weak-form solutions can significantly improve the quality of wavefield
 194 decomposition, which is the basis for the following imaging tests. The deviations of Equa-
 195 tions 7 and 8 can be found in the supplementary material.

197 **2.3 The workflow for passive source RTM**

198 The implementation of passive source RTM can be summarised in the following four
 199 steps:

- 200 1. Teleseismic data preprocessing. During this step, we estimate source time functions
 201 for each teleseismic event based on the principle component analysis for the aligned
 202 incident waves (Bostock & Rondenay, 1999; Shang et al., 2017), such as P, S or
 203 SKS waves. For this purpose, the incident waves are aligned according to the on-
 204 set time of the incident phases estimated using the TauP package (Crotwell et al.,
 205 1999). Then, an iterative time deconvolution (Kikuchi & Kanamori, 1982) is ap-
 206 plied to each component of original(unaligned) data to remove the source time func-
 207 tion, followed by bandpass filtering for later finite frequency simulations.
- 208 2. Injecting the preprocessed teleseismic data for the SEM solver as adjoint sources
 209 to the acceleration vector. Given the linear relation between the source time func-
 210 tion and wavefield, this step further avoids obtaining the double integral of the
 211 teleseismic data, which should be injected to construct the second time integral
 212 of the displacement wavefield indicated by Equation 4.
- 213 3. During the reverse time wavefield propagation, solving the weak-form solutions
 214 shown in Equations 7 and 8 to get vector wavefields $\mathbf{u}_{i_e}^P$ and $\mathbf{u}_{i_e}^S$, followed by ap-
 215 plying the zero-lag cross-correlation imaging condition (Equation 1), noted as $\mathbf{I}_{i_e}^{PS}$.
 216 To save computational costs, one may consider performing wavefield separation
 217 for every several time steps according to the Nyquist rule. We also apply the imag-
 218 ing condition to $\mathbf{u}_{i_e}^P$ with $\mathbf{u}_{i_e}^P$ to get the PP image as $\mathbf{I}_{i_e}^{PP}$.
- 219 4. Sum all corresponding event images to obtain \mathbf{I}_{PS} and \mathbf{I}_{PP} , and then get the im-
 220 age with $\mathbf{I}_{PS} = \frac{\mathbf{I}_{PS}}{\mathbf{I}_{PP} + \epsilon}$ to compensate for energies at great depths. Here, ϵ is a
 221 small damping value used to avoid dividing by zeros.

222 **3 Applications**

223 In this section, we use two synthetic tests and one real data example to validate
 224 our method based on linear array recordings although we are using 3-D modeling and
 225 migration. It is well-known that station spacing together with the data frequency are
 226 important factors that may result in spatial aliasing during passive source RTM (Gray,
 227 2013; Shang et al., 2012). Therefore, most teleseismic migration methods used to image

lithospheric structures rely on dense arrays (station spacing is \sim 5 km) (Bostock, 1998; Rondenay et al., 2000; Rondenay, 2009; Shang et al., 2017). Therefore, all synthetic simulations in our tests are implemented using a 3-D plane-wave injection method, FK-SEM (Tong, Komatitsch, et al., 2014; Tong, Chen, et al., 2014) and recorded by a dense linear array. Then, passive source RTM is implemented based on 3-D migration. We note here, there are mainly three advantages to implement 3-D rather than 2-D migration even using recordings from a linear array: 1) no 3-D/2-D transformation is needed (“Line-source simulation for shallow-seismic data. Part 1: Theoretical background, author=Forbriger, Thomas and Groos, Lisa and Schäfer, Martin”, 2014; Schäfer et al., 2014; C. Zhang et al., 2018), which is important to correct phase and amplitude differences between 3-D and 2-D simulations; 2) more teleseismic events can be chosen for real data applications; 3) no needs to project stations onto a line, which is required for 2-D migration even with linear arrays because their locations are not critically located on 2-D linear mesh grid (Shang et al., 2017).

3.1 Synthetic test 1: effects of topographic variations

The first synthetic test is used to highlight the effects of topographic variations on passive source migration when using high-frequency teleseismic data. The input model is a two-layer model with an interface at 30 km depth. The density, V_p and V_s for the first layer between 0 and 30 km depth are 2.72 g/cm³, 5.8 km/s and 3.46 km/s, which are 3.423 g/cm³, 8.06 km/s and 4.53 km/s between 30 and 60 km depths. These values are taken from the AK135 model (Kennett et al., 1995). The simulation domain spans -90 to 90 km along the X (longitude) direction, -60 to 60 km along the Y (latitude) direction and 0 to 60 km along the depth direction. The element size is 1.0 km, which allows for the wavefield simulation with the highest frequency around 3.0 Hz. The Stacey absorption boundary condition is used for each face of the model except for the top, which is a free-surface boundary condition for our simulations (Mahrer, 1990). A 1.5-D topographic change (no change along the Y direction) following the solid line shown in Figure 4b is designed to validate its effects on passive source RTM. We note here, the model will be stretched in depth direction within the SPECFEM package to handle the topographic changes. 161 stations with a horizontal station spacing of 1.0 km are distributed on the surface of the model. We use a Ricker source wavelet with a peak frequency of 1.0 Hz to initialize the incident plane waves. 12 P-wave plane waves, with incident an-

gles ranging from 12° - 27° , are injected into the local simulation domain to simulate the telesismic waves. The back-azimuthal angles for events 1, 3, 7, 9 and 11 are 90° and 270° for the rest events. This makes a symmetric coverage of plane waves propagating through the model. The corresponding telesismic data are recorded by the station for each event. Seismograms for the first telesismic event with an incident angle of 27° and the back-azimuthal angle of 90° are shown in Figure 3. By using the short-time average over long-time average (STA/LTA) algorithm (Withers et al., 1998), it is feasible to detect the onset of the incident wavefield. The magenta lines in Figure 3 denote the time windows used in our imaging, which are 5 seconds before and 6 seconds after the onset of the incident P waves. It helps us to isolate multiple refections that may distort our imaging results. We speculate that the onset of incident P waves in both Z and X components shows the imprint of the topographic changes. Without considering the topographic changes, i.e., injecting telesismic data at 0 km elevation of each station, a significant imprint of topography can be observed in the imaging result in Figure 4a, which looks like a mirror of the topography. On the contrary, the reflector can be accurately imaged by injecting the telesismic data at the right locations by considering the topographic changes (Figure 4b).

3.2 Synthetic test 2: imaging subduction slabs

In this synthetic test, we validate the capability of our method to image complex structures in subduction zones. The background model is a two-layer crust and mantle structure, with density, Vp and Vs, the same as the previous example. A 3-D subducting slab (Figure 6a-b) is designed between -60 to 60 km along the X (Longitude) direction, -30 to 30 km along the Y (Latitude) direction and 40 to 140 km in depth with a thickness of 50 km. The Moho depth is 35 km. The model parameters (density, Vp and Vs) of the subducting slab are 12% greater than the background model. Our simulation domain spans from -120 to 120 km along the X direction, -48 to 48 km along the Y direction and 0 to 160 km along the depth direction. We use 201 stations with 1.0 km station spacing evenly distributed from -100.0 km to 100.0 km. 12 telesismic P wave events with the same back-azimuth and incident angles as the previous example are injected into the local study region, starting from an initial depth at 240 km. The rest parameters are the same as the previous synthetic test. Synthetic Z and X component seismograms for the first telesismic event are illustrated in Figures 5a and b. Because the back-

azimuth angle of this event is 90° , the X components are equal to the radial components, which could be used to investigate Ps-converted waves. Due to the complexity of the velocity model, we speculate several kinds of multiple reflections (Moho and slab-related) for the P waves in Z components. The corresponding Ps-converted waves can be investigated from X components in Figure 5b. Interestingly, despite being weaker than Moho-related converted waves (S), slab-related as well as multiple reflection-related S-converted waves can also be seen.

Our RTM is implemented using a smoothed two-layer background model (Figures 6 c-d) to avoid artifacts arising from sharp velocity interfaces during the wavefield separation (J. Yang et al., 2018). It is smoothed vertically using a Gaussian function with a radius of 5.0 km. This means we do not include the slab in our migration velocity model, which is close to the real cases. After stacking and illuminating, the interfaces of the slab are well imaged as displayed in Figure 6g. It suggests that our method is capable of imaging complex structures, such as velocity anomalies with high dipping angles. Because it is quite difficult to isolate multiple reflections in this case, we also see different-order multiple imaging artifacts in our stacked result. We also show the imaging result from the first four teleseismic events, which also successfully captures the main features of the slab and the Moho, but with stronger artifacts due to not enough stacking. In addition, the images along the Y (Latitude) direction (Figures 6f and h), which is perpendicular to our stations' distribution, indicate that with only several effective stations, the migration will map the converted waveforms along the isochrone interfaces in depths (Schneider, 1978). Because we only use one linear array across the slab, it is necessary to consider the contributions of teleseismic events with back-azimuthal angles away from the array direction. We test another three back-azimuthal angle pairs, which are $0^\circ/180^\circ$, $45^\circ/225^\circ$ and $135^\circ/315^\circ$ with the same incident angle as the previous test. Figure 7 shows the migration results from the back-azimuthal angle pairs of $0^\circ/180^\circ$ and $45^\circ/225^\circ$. The migration result from $135^\circ/315^\circ$ azimuthal-angle pair is similar to the one from $45^\circ/225^\circ$. As expected, when the azimuthal angles are away from the linear array direction, the interfaces of the imaged slab and the Moho become weaker and more incoherent artifacts become stronger. Interestingly, the Moho interface disappears when using teleseismic events with the $0^\circ/180^\circ$ azimuthal pair. This could be explained by the concept of the Fresnel zone. Bostock (1998) pointed out that the Fresnel zone of the scattering points depends on the dominant frequencies and depths of the interface. Assuming that con-

325 structive interference arises for phase differences less than a quarter period, the diam-
 326 eter of the Fresnel zone around the interface varies between ~ 25 km for P_mS (Moho con-
 327 verted wave) at 0.5 Hz to ~ 160 km for $P_{660}S$ (generated at the 660 km discontinuity)
 328 at 0.25 Hz. This means the converted waves recorded at stations that arise from deeper
 329 interfaces (e.g., X=0, Y=0 and Z=660 km) could be the response to a larger range of
 330 interfaces, e.g., X=[-80, 80], Y=[-80, 80], Z=[580, 740] km. We note here, the estima-
 331 tions of X and Y ranges are fairly rough. For teleseismic events with back-azimuthal an-
 332 gles away from the linear array, their Fresnel zone is also away from the structures be-
 333 neath the linear array. As a consequence of small Fresnel zones, shallow interfaces, such
 334 as the Moho, gradually disappear beneath the linear array due to incoherence stacking
 335 from different events. Therefore, reasonable good station, incident angle and azimuthal
 336 angle coverages are preferred for our method if we intend to image the interfaces beneath
 337 a linear array (Shang et al., 2012; Li et al., 2018).

338 **3.3 Imaging the Cheyenne Belt suture zone (CBSZ) using the Laramie**
 339 **array**

340 ***3.3.1 Geological setting***

341 The CBSZ is a tectonic suture zone between the Archean Wyoming craton to the
 342 north and the Paleoproterozoic Yavapai province to the south (Karlstrom & Houston,
 343 1984; Sims & Stein, 2003; Hansen & Dueker, 2009; Jones et al., 2010). It contains a set
 344 of steeply south-dipping shear zones formed during the 1.78–1.75 Ga Medicine Bow orogeny
 345 when the Proterozoic Green Mountain arc collided with the passive margin of the Wyoming
 346 craton via south-facing subduction (Tyson et al., 2002; Hansen & Dueker, 2009). Steep
 347 stretching lineations and shear-sense features indicate south-side-up motion (Tyson et
 348 al., 2002; Hansen & Dueker, 2009). To better constrain the structure of the CBSZ, the
 349 Laramie array was deployed within the Laramie basin across the inferred trace of the
 350 Cheyenne belt (Figure 8) (Hansen & Dueker, 2009). It is a dense 80 km long linear ar-
 351 ray with broadband seismometers, which consists of 30 sensors spaced 2.2 km apart and
 352 was deployed for a period of eight months in 2000–2001. Based on P and S receiver func-
 353 tions together with teleseismic P wave travelttime tomography, Hansen and Dueker (2009)
 354 found an imbricated Moho north of the Cheyenne belt. It is basically consistent with the
 355 interpretation of seismic results from the CDROM (Continental Dynamics Rocky Moun-
 356 tain) project (Tyson et al., 2002). However, either due to the limited aperture of the Laramie

array, or the methodologies, the CBSZ hasn't been clearly imaged as shown in Figure 7 of Hansen and Dueker (2009). Ruigrok et al. (2010) used seismic interferometry to extract reflection responses from the coda of the transmitted energy from distant earthquakes, where they found discontinuities in their migration images, which were interpreted as the CBSZ. Here, we use our passive source RTM method to further investigate the detailed shape of the CBSZ with converted teleseismic P and S waves.

363 ***3.3.2 Data***

364 The teleseismic P wave dataset is constructed from 11 events at 30°–90° distance
 365 with body-wave magnitudes greater than 5.5. The S wave dataset is selected from 1 S-
 366 wave and 7 SKS events from 55°–85° and 85°–120° epicentral distances, respectively (Wilson
 367 & Aster, 2005; Yuan et al., 2006). Detailed information about these events can be found
 368 in Table 1 and displayed in Figure 9. The data is selected, downloaded and preprocessed
 369 with the standing order for data package (SOD) (Owens et al., 2004). For each P wave
 370 event, three-component waveforms within the time window of two minutes before and
 371 three minutes after direct P arrivals predicted by the AK135 model (Kennett et al., 1995)
 372 are collected. The north-south and west-east component seismograms are rotated to ra-
 373 dial and transverse components after removing instrument response, linear trend, and
 374 mean values, followed by a bandpass filter of 1–20 s. Then, the preprocessed three-component
 375 waveforms of each event are visually inspected, and only those with a signal-to-noise ra-
 376 tio (SNR) larger than 3.0 and 2.0 for vertical and radial components are kept. Afterward,
 377 we use the open-source software AIMBAT (Lou et al., 2013) to remove bad seismograms
 378 with spurious amplitudes and cross-correlation coefficients lower than 0.80 for vertical
 379 and radial components. To avoid spatial aliasing, only events with more than 15 seis-
 380 mograms are remained. The data selection process for S and SKS events is similar ex-
 381 cept: (1) the time window is defined as two minutes before and three minutes after in-
 382 cident S arrivals; (2) seismograms with SNR larger than 2.0 and 3.0 for vertical and ra-
 383 dial components are kept. This is because S waves are mainly in radial components. In
 384 the end, most events have more than 25 high-quality seismograms for each component.

385 Gray (2013) and Li et al. (2018) suggested that station spacing is an important fac-
 386 tor for spatial aliasing during passive source RTM. For example, 5 km station spacing
 387 will result in slightly aliased P-wave migration with 1 Hz data, given the incident an-
 388 gles range from 12° to 27°. Therefore, we interpolate those deleted bad seismograms

389 using 2-D cubic-spline interpolation (J. Zhang & Zheng, 2015). The 2-D cubic-spline in-
 390 terpolation was originally used to refine the receiver functions from sparse station dis-
 391 tributions. Here, we use it to interpolate the aligned vertical and radial component seis-
 392 mograms. It mainly includes three steps: (1) align the seismograms according to the on-
 393 set of incident waves (P or S), predicted by the reference model, such as AK135 (Kennett
 394 et al., 1995). The reference time could be further adjusted by applying a multichannel
 395 cross-correlation algorithm (VanDecar & Crosson, 1990); (2) perform 2-D interpolation
 396 for each time step using the cubic-spline method for each component; (3) shift the in-
 397 terpolated data back according to the reference time. We note here, the absolute am-
 398 plitudes are kept during interpolation for each channel and component, which is differ-
 399 ent from J. Zhang and Zheng (2015). This is important for dealing with multi-component
 400 data. As compared in Figure 9, the interpolated seismograms follow the same trend of
 401 nearby stations in great details for both P and S waves. We use 10 s before and 30 s af-
 402 ter the onset of P and 30 s before and 30 s after the onset of S waves for the following
 403 migration.

404 ***3.3.3 Migration***

405 Our computational domain for wavefield propagation spans from -106.25° to -105.30°
 406 along longitude, 40.85° to 41.75° along latitude, and -10 to 110 km in the depth direc-
 407 tion. We use 48, 60 and 80 elements along these three directions, yielding an average el-
 408 ement size of 1.5 km. Given the minimal Vp of 5.05 km/s from our migration model and
 409 about two elements for each P wavelength, it allows us to use periods greater than 0.65
 410 s for accurate wave simulation. A 7.5 km (about 3 elements) perfect-matched layer (PML)
 411 absorbing boundary condition is applied to each surface of the simulation domain to avoid
 412 artificial reflections from the boundaries (Komatitsch & Tromp, 2003). As outlined in
 413 section 2.3, source time functions are estimated from the aligned vertical component of
 414 each P wave event (radial for S wave), followed by an iterative time deconvolution (Kikuchi
 415 & Kanamori, 1982) to remove the source time function effect (Bostock, 1998; Rondenay
 416 et al., 2000; Bostock et al., 2001; Bostock, 2002; Shang et al., 2017). Given an average
 417 station spacing about 2-3 km, the deconvolved event data are bandpass filtered at 1-20
 418 s as the adjoint sources for finite frequency wavefield modeling. The migration velocity
 419 model is extracted from a 3-D regional model US2016 (Shen & Ritzwoller, 2016). We
 420 smooth it using a Gaussian function with a radius of 5.0 km both vertically and hori-

421 zontally. Then, the migration is implemented for each event and summed up to get the
 422 final stacked image. In this study, we perform the migration for P and S waves separately.

423 **3.3.4 Results**

424 Due to the finite frequency property, we identify velocity increase as positive mi-
 425 gration phases flanked by negative ones as indicated by synthetic tests (Figures 4 and
 426 6). The basement-sediment contact beneath the Laramie basin is identified in the P-wave
 427 image as the positive high amplitude phases beneath the negative phases around 2-7 km
 428 (Figure 10a), which becomes slightly deeper (dip to the northwest) between 30-40 km
 429 in the horizon, right beneath the Laramie basin. Whereas this feature is not clear from
 430 the S wave image shown in Figure 10b, possibly due to the back azimuthal angles of most
 431 S events being basically perpendicular to the array direction (Figure 9d). The most promi-
 432 nent features in both P and S wave images are the bunches of south-dipping positive/negative
 433 phases between -40 and 10 km in lateral direction and 0 and 70 km in depths. They are
 434 interpreted as the CBSZ, which situated juxtaposition of accreted Proterozoic terranes
 435 with the Archean Wyoming craton (Hansen & Dueker, 2009; Tyson et al., 2002). The
 436 northward crustal thickening seems to be indicated by the Proterozoic Moho, highlighted
 437 by dark green dots in the P wave image (Figure 10a). However, due to spatial aliasing
 438 in both P and S wave images between 20 and 40 km horizontally, the Archean Moho is
 439 not well constrained (Hansen & Dueker, 2009). Therefore, we try to suppress the spa-
 440 tial aliasing effect by refining the stations for every 1.0 km as illustrated in Figure 11.
 441 The comparison of the interpolated seismograms shows a good match both in trends and
 442 amplitudes of different events. We conduct P wave migration again using the refined data.
 443 As shown in Figure 11c, most spatial aliasing artifacts are suppressed and both the Archean
 444 Moho (\sim 45 km) and the Proterozoic Moho (\sim 60 km) can be clearly identified. They are
 445 slightly dipping northward to the north of the CBSZ. These are consistent with previ-
 446 ous studies (Allmendinger et al., 1982; Prodehl et al., 1989; Snelson et al., 1998; Moro-
 447 zova et al., 2002). However, our Proterozoic Moho seems to be distorted with the CBSZ
 448 around 15 km in the horizontal direction (south of the CBSZ), whereas Hansen and Dueker
 449 (2009) found it to be continuous beneath the entire array. Nevertheless, we interpreted
 450 the CBSZ as the orange shadow zones in Figure 11c. Further investigation for a detailed
 451 migration velocity model will be helpful for better imaging and interpretation.

452 **4 Discussions**

453 We combine full wavefield passive source RTM with the spectral element method
 454 so that it is convenient to handle topographic changes and velocity heterogeneities. Both
 455 synthetic and suture zone imaging examples demonstrate the performance of our method.

456 **4.1 2-D data interpolation**

457 Migration antialiasing due to spatial frequency components (station spacing) is a
 458 longstanding problem in seismic imaging, for example, 5-D data interpolation (Trad, 2009)
 459 has been developed to improve the imaging quality. Therefore, it is important to con-
 460 sider the effects of station spacing for passive RTM (L. Chen et al., 2005; Li et al., 2018).
 461 The Nyquist-Shannon sampling theorem suggests that the station spacing is required to
 462 be smaller than the apparent half-wavelength to fully construct the wavefield from recorded
 463 seismograms at the surface (Gray, 2013; Li et al., 2018). Therefore, given constant crustal
 464 P and S wave velocities of 5.8 and 3.2 km/s, respectively, and incident angles of 12° to
 465 27°, full construction of 1.0 Hz P waves at near-surface requires a station spacing rang-
 466 ing from 6.4 to 14.5 km, but 3.5 to 8.0 km for 1.0 Hz S waves. This gives us an upper
 467 bound limit for the station spacing. Smaller station spacing is expected because the in-
 468 cident angle for converted Ps waves could be larger, especially when the subsurface struc-
 469 tures are complex, like subduction and suture zones. For example, given a high-frequency
 470 cut about 2.5 Hz, a 2.0 km station spacing would result in slight spatial aliasing as shown
 471 in Figure 12a compared to the result obtained with a 1.0 km station spacing shown in
 472 Figure 6g. As expected, a 4.0 km station spacing would result in even stronger spatial
 473 aliasing as shown in Figure 12b. Depending on the specific imaging target, 2-D data in-
 474 terpolation might be necessary for migration. However, most data interpolation (regu-
 475 larization) strategies developed for seismic exploration, like FX domain trace interpo-
 476 lation (Spitz, 1991), antileakage Fourier transformation (Xu et al., 2005) or curvelet trans-
 477 formation (Herrmann & Hennenfent, 2008; Shang et al., 2017) require linearity of sta-
 478 tion distributions, which is not straightforward to handle 2-D irregularly-spaced (3-D if
 479 we consider the station elevations) data. Therefore, we prefer to use the 2-D cubic-spline
 480 interpolation (J. Zhang & Zheng, 2015) or the radial function-based method (Shepard,
 481 n.d.), which can naturally handle irregularly-spaced data for our migration. We note here
 482 that, unlike its first application for interpolating 2-D receiver functions (J. Zhang & Zheng,
 483 2015), we need to align the multi-channel data prior to interpolation for each component,

484 and then shift the interpolated data back according to the onsets of incident waves for
 485 migration.

486 4.2 Source time function estimations

487 It is straightforward to estimate the source time functions for P waves, which has
 488 been successfully used for teleseismic full waveform inversion (Y. Wang et al., 2016; K. Wang
 489 et al., 2021). However, the estimation of source time functions for S waves should be care-
 490 fully considered, because of relatively larger incident angles compared to P waves. This
 491 results in the leakage of S waves into vertical and transverse components. Therefore, ro-
 492 tation of vertical, radial and transverse components into P, SV and SH polarization di-
 493 rections could be helpful for source time function estimations for S waves (Bostock, 1998;
 494 Rondenay, 2009).

495 4.3 Migration velocity models

496 One advantage of our methodology is that we are able to implement migration based
 497 on 3-D velocity models with strong heterogeneities. The accuracy of migration velocity
 498 models is essential for mapping seismograms to correct locations and avoiding stacking
 499 artifacts (Mora, 1989; He & Liu, 2020). To illustrate the advantages of using more ac-
 500 curate migration velocity models for imaging, we conduct another migration for slab imag-
 501 ing, which is shown in Figure 13. The migration velocity model is obtained by smooth-
 502 ing the true velocity model using a Gaussian function with a radius of 5.0 km both hor-
 5031zontally and vertically. We speculate that, with a more reasonable migration velocity
 504 model, the vertical boundaries (see true model in Figure 6a) on the left and right sides
 505 of the slab are better constrained compared to those shown in Figure 6g. However, for
 506 our suture zone imaging, a smoothed regional 3-D model is not accurate enough because
 507 the grid spacing (~ 25 km) of model US2016 (Shen & Ritzwoller, 2016) is too large to
 508 capture velocity heterogeneities in such a small study region. Therefore, teleseismic body
 509 wave travelttime tomography (D. Zhao et al., 1992; Tong, 2021) or ambient noise tomog-
 510 raphy (C. Zhang et al., 2018) could be used to construct a more reasonable migration
 511 velocity model for our imaging in the future.

512 **5 Conclusion**

513 In this study, we propose to solve weak-form solutions to decompose elastic wave-
 514 fields into vector P and S waves for teleseismic reverse time migration based on the spec-
 515 tral element method. Both synthetic tests and Cheyenne Belt suture zone imaging demon-
 516 strate the capability of our method to image complex structures with strong velocity het-
 517 erogeneity. For linear array migration, our synthetic tests show that teleseismic events
 518 with back azimuthal angles parallel to the linear array direction contribute more to sub-
 519 surface migration images than those away from the linear array direction. However, the
 520 latter could still contribute to the image beneath the array thanks to larger Fresnel zone
 521 contributions at greater depths. In addition, we reveal several south-dipping structures
 522 in the Laramie basin, which are interpreted as the Cheyenne Belt suture zone, and are
 523 consistent with geological interpretations from previous studies. For better performance
 524 of the migration-based imaging method, 2-D/3-D data interpolation is required to avoid
 525 spatial aliasing during the construction of wavefields in the subsurface.

526 **Open Research**

527 The Laramie array seismic data used in this study can be obtained from the IRIS
 528 Data Management Center (<https://ds.iris.edu/ds>) under the network codes XF. We
 529 use SPECFEM3-D Cartesian 4.0.0 (Komatitsch et al., 1999; Komatitsch & Tromp, 2002b,
 530 2002a) published under the GPL 3 license for synthetic and real data simulations. PyGMT
 531 (Wessel et al., 2019) download from (<https://www.pygmt.org/latest/>) is used to plot
 532 figures.

533 **Acknowledgments**

534 This paper is contribution no. *** from the Department of Geosciences at the Uni-
 535 versity of Texas at Dallas. The numerical results are computed through the Optane nodes
 536 on the UTD Seismology Group HPC clusters. This research is partially supported by
 537 the sponsors of the UT Dallas 3D + 4D Seismic Full Waveform Inversion research con-
 538 sortium.

539 **Author Contributions**

540 The authors confirm their contribution to the paper as follows: study conception
 541 and design: Hejun Zhu; Weak-form solutions were first proposed by Yu Chen, then the-
 542 oretically derivated and tested by Bin He. Data collection: Bin He; Analysis and inter-
 543 pretation of results: Bin He, Hejun Zhu, David Lumley, Qinya Liu, Hitoshi Kawakatsu
 544 and Nozomu Takeuch; Draft manuscript preparation: Bin He, Hejun Zhu. All authors
 545 review the results and approve the final version of the manuscript.

546 **References**

- 547 Ai, Y., Chen, Q.-f., Zeng, F., Hong, X., & Ye, W. (2007). The crust and upper
 548 mantle structure beneath southeastern China. *Earth and Planetary Science
 Letters*, 260(3-4), 549–563.
- 549 Allmendinger, R., Brewer, J., Brown, L., Kaufman, S., Oliver, J., & Houston, R.
 550 (1982). COCORP profiling across the Rocky Mountain Front in south-
 551 ern Wyoming, Part 2: Precambrian basement structure and its influence on
 552 Laramide deformation. *Geological Society of America Bulletin*, 93(12), 1253–
 553 1263.
- 554 Andrade, P. N., Pestana, R. C., & dos Santos, A. W. (n.d.). Kirchhoff depth
 555 migration using maximum amplitude traveltimes computed by the Cheby-
 556 shev polynomial recursion. In *14th International Congress of the Brazilian
 557 Geophysical Society & EXPOGEF, Rio de Janeiro, Brazil, 3-6 August 2015,*
 558 *pages=1109–1113, year=2015, organization=Brazilian Geophysical Society.*
- 559 Audebert, F., Nichols, D., Rekdal, T., Biondi, B., Lumley, D. E., & Urdaneta, H.
 560 (1997). Imaging complex geologic structure with single-arrival Kirchhoff
 561 prestack depth migration. *Geophysics*, 62(5), 1533–1543.
- 562 Banerdt, W. B., Smrekar, S. E., Banfield, D., Giardini, D., Golombek, M., Johnson,
 563 C. L., ... others (2020). Initial results from the InSight mission on Mars.
 564 *Nature Geoscience*, 13(3), 183–189.
- 565 Baysal, E., Kosloff, D. D., & Sherwood, J. W. (1983). Reverse time migration. *Geo-
 566 physics*, 48(11), 1514–1524.
- 567 Bevc, D. (1997). Flooding the topography: Wave-equation datuming of land data
 568 with rugged acquisition topography. *Geophysics*, 62(5), 1558–1569.
- 569 Bostock, M. (1998). Mantle stratigraphy and evolution of the Slave province. *Jour-*

- 571 *nal of Geophysical Research: Solid Earth*, 103(B9), 21183–21200.
- 572 Bostock, M. (2002). Kirchhoff-approximate inversion of teleseismic wavefields. *Geo-*
 573 *physical Journal International*, 149(3), 787–795.

574 Bostock, M., & Rondenay, S. (1999). Migration of scattered teleseismic body waves.
 575 *Geophysical journal international*, 137(3), 732–746.

576 Bostock, M., Rondenay, S., & Shragge, J. (2001). Multiparameter two-dimensional
 577 inversion of scattered teleseismic body waves 1. Theory for oblique incidence.
 578 *Journal of Geophysical Research: Solid Earth*, 106(B12), 30771–30782.

579 Burdick, L. J., & Langston, C. A. (1977). Modeling crustal structure through the
 580 use of converted phases in teleseismic body-wave forms. *Bulletin of the Seismo-*
 581 *logical Society of America*, 67(3), 677–691.

582 Burridge, R., de Hoop, M. V., Miller, D., & Spencer, C. (1998). Multiparameter in-
 583 version in anisotropic elastic media. *Geophysical Journal International*, 134(3),
 584 757–777.

585 Chen, L., Wen, L., & Zheng, T. (2005). A wave equation migration method for
 586 receiver function imaging: 1. Theory. *Journal of Geophysical Research: Solid*
 587 *Earth*, 110(B11).

588 Chen, X., Li, Y., & Levin, V. (2018). Shear wave splitting beneath eastern
 589 North American continent: evidence for a multilayered and laterally vari-
 590 able anisotropic structure. *Geochemistry, Geophysics, Geosystems*, 19(8),
 591 2857–2871.

592 Cheng, C., Bodin, T., & Allen, R. M. (2016). Three-dimensional pre-stack depth
 593 migration of receiver functions with the fast marching method: a Kirchhoff
 594 approach. *Geophysical Journal International*, 205(2), 819–829.

595 Claerbout, J. F. (1985). *Imaging the earth's interior* (Vol. 1). Blackwell Scientific
 596 Publications Oxford.

597 Clayton, R., Persaud, P., Denolle, M., & Polet, J. (2019). Exposing Los Angeles's
 598 shaky geologic underbelly, Eos, 100. *EOS*. <https://doi.org/10.1029>.

599 Crotwell, H. P., Owens, T. J., Ritsema, J., et al. (1999). The TauP Toolkit: Flex-
 600 ible seismic travel-time and ray-path utilities. *Seismological Research Letters*,
 601 70, 154–160.

602 Duan, C., Lumley, D., & Zhu, H. (2021). Estimation of micro-earthquake source
 603 locations based on full adjoint P and S wavefield imaging. *Geophysical Journal*

- 604 *International*, 226(3), 2116–2144.
- 605 Dueker, K. G., & Sheehan, A. F. (1997). Mantle discontinuity structure from mid-
606 point stacks of converted P to S waves across the Yellowstone hotspot track.
607 *Journal of Geophysical Research: Solid Earth*, 102(B4), 8313–8327.
- 608 Fichtner, A. (2010). *Full seismic waveform modelling and inversion*. Springer Sci-
609 ence & Business Media.
- 610 Fichtner, A., Kennett, B. L., Igel, H., & Bunge, H.-P. (2009). Full seismic wave-
611 form tomography for upper-mantle structure in the Australasian region using
612 adjoint methods. *Geophysical Journal International*, 179(3), 1703–1725.
- 613 Gilbert, H. J., Sheehan, A. F., Dueker, K. G., & Molnar, P. (2003). Receiver func-
614 tions in the western United States, with implications for upper mantle struc-
615 ture and dynamics. *Journal of Geophysical Research: Solid Earth*, 108(B5).
- 616 Gray, S. H. (2013). Spatial sampling, migration aliasing, and migrated amplitudes.
617 *Geophysics*, 78(3), S157–S164.
- 618 Gray, S. H., & May, W. P. (1994). Kirchhoff migration using eikonal equation travel-
619 times. *Geophysics*, 59(5), 810–817.
- 620 Hansen, S., & Dueker, K. (2009). P-and S-wave receiver function images of crustal
621 imbrication beneath the Cheyenne Belt in southeast Wyoming. *Bulletin of the*
622 *Seismological Society of America*, 99(3), 1953–1961.
- 623 He, B., & Liu, Y. (2020). Wave-equation migration velocity analysis using Radon-
624 domain common-image gathers. *Journal of Geophysical Research: Solid Earth*,
625 125(2), e2019JB018938.
- 626 Herrmann, F. J., & Hennenfent, G. (2008). Non-parametric seismic data recovery
627 with curvelet frames. *Geophysical Journal International*, 173(1), 233–248.
- 628 Hill, N. R. (1990). Gaussian beam migration. *Geophysics*, 55(11), 1416–1428.
- 629 Hill, N. R. (2001). Prestack Gaussian-beam depth migration. *Geophysics*, 66(4),
630 1240–1250.
- 631 Jin, H., & Etgen, J. (n.d.). Evaluating Kirchhoff migration using wave-equation
632 generated maximum amplitude traveltimes. In *SEG Technical Program Ex-*
633 *panded Abstracts 2020*, pages=2968–2972, year=2020, publisher=Society of
634 Exploration Geophysicists.
- 635 Jones, D. S., Snook, A. W., Premo, W. R., & Chamberlain, K. R. (2010). New mod-
636 els for Paleoproterozoic orogenesis in the Cheyenne belt region: Evidence from

- 637 the geology and U-Pb geochronology of the Big Creek Gneiss, southeastern
638 Wyoming. *Bulletin*, 122(11-12), 1877–1898.
- 639 Karlstrom, K., & Houston, R. (1984). The Cheyenne belt: Analysis of a Proterozoic
640 suture in southern Wyoming. *Precambrian research*, 25(4), 415–446.
- 641 Kawakatsu, H., & Watada, S. (2007). Seismic evidence for deep-water transportation
642 in the mantle. *Science*, 316(5830), 1468–1471.
- 643 Kennett, B. L., Engdahl, E., & Buland, R. (1995). Constraints on seismic velocities
644 in the Earth from traveltimes. *Geophysical Journal International*, 122(1), 108–
645 124.
- 646 Kikuchi, M., & Kanamori, H. (1982). Inversion of complex body waves. *Bulletin of*
647 *the Seismological Society of America*, 72(2), 491–506.
- 648 Kind, R., Yuan, X., & Kumar, P. (2012). Seismic receiver functions and the
649 lithosphere-asthenosphere boundary. *Tectonophysics*, 536, 25–43.
- 650 Knapmeyer-Endrun, B., Bissig, F., Compaire, N., Garcia, R., Joshi, R., Khan, A.,
651 ... others (2020). First seismic constraints on the Martian crust-receiver
652 functions for InSight.
- 653 Komatitsch, D., & Tromp, J. (2002a). Spectral-element simulations of global seis-
654 mic wave propagation—II. Three-dimensional models, oceans, rotation and
655 self-gravitation. *Geophysical Journal International*, 150(1), 303–318.
- 656 Komatitsch, D., & Tromp, J. (2002b). Spectral-element simulations of global seismic
657 wave propagation—I. Validation. *Geophysical Journal International*, 149(2),
658 390–412.
- 659 Komatitsch, D., & Tromp, J. (2003). A perfectly matched layer absorbing boundary
660 condition for the second-order seismic wave equation. *Geophysical Journal In-*
661 *ternational*, 154(1), 146–153.
- 662 Komatitsch, D., & Vilotte, J.-P. (1998). The spectral element method: an efficient
663 tool to simulate the seismic response of 2D and 3D geological structures. *Bul-*
664 *letin of the seismological society of America*, 88(2), 368–392.
- 665 Komatitsch, D., Vilotte, J.-P., Vai, R., Castillo-Covarrubias, J. M., & Sánchez-
666 Sesma, F. J. (1999). The spectral element method for elastic wave equa-
667 tions—application to 2-D and 3-D seismic problems. *International Journal for*
668 *numerical methods in engineering*, 45(9), 1139–1164.
- 669 Langston, C., & Corvallis, O. (1977). crustal and upper mantle receiver structure

- 670 from teleseismic P-waves and S-waves. *Bull. Seismol. Soc. Am.*, *67*, 713–724.
- 671 Levander, A., Niu, F., Symes, W. W., & Nolet, G. (2005). Imaging teleseis-
672 mic P to S scattered waves using the Kirchhoff integral. *GEOPHYSICAL
673 MONOGRAPH-AMERICAN GEOPHYSICAL UNION*, *157*, 149.
- 674 Li, J., Shen, Y., & Zhang, W. (2018). Three-dimensional passive-source reverse-time
675 migration of converted waves: The method. *Journal of Geophysical Research:
676 Solid Earth*, *123*(2), 1419–1434.
- 677 Line-source simulation for shallow-seismic data. Part 1: Theoretical background,
678 author=Forbriger, Thomas and Groos, Lisa and Schäfer, Martin. (2014).
679 *Geophysical Journal International*, *198*(3), 1387–1404.
- 680 Liu, K., & Levander, A. (2013). Three-dimensional Kirchhoff-approximate gener-
681 alized Radon transform imaging using teleseismic P-to-S scattered waves. *Geo-
682 physical Journal International*, *192*(3), 1196–1216.
- 683 Lognonné, P., Banerdt, W. B., Pike, W., Giardini, D., Christensen, U., Garcia,
684 R. F., ... others (2020). Constraints on the shallow elastic and anelastic struc-
685 ture of Mars from InSight seismic data. *Nature Geoscience*, *13*(3), 213–220.
- 686 Long, M. D., Benoit, M. H., Aragon, J. C., & King, S. D. (2019). Seismic imaging of
687 mid-crustal structure beneath central and eastern North America: Possibly the
688 elusive Grenville deformation? *Geology*, *47*(4), 371–374.
- 689 Lou, X., Van Der Lee, S., & Lloyd, S. (2013). AIMBAT: A python/matplotlib tool
690 for measuring teleseismic arrival times. *Seismological Research Letters*, *84*(1),
691 85–93.
- 692 Maguire, R., Schmandt, B., Li, J., Jiang, C., Li, G., Wilgus, J., & Chen, M. (2022).
693 Magma accumulation at depths of prior rhyolite storage beneath Yellowstone
694 Caldera. *Science*, *378*(6623), 1001–1004.
- 695 Mahrer, K. D. (1990). Numerical time step instability and Stacey's and Clayton-
696 Engquist's absorbing boundary conditions. *Bulletin of the Seismological Soci-
697 ety of America*, *80*(1), 213–217.
- 698 McMechan, G. A. (1982). Determination of source parameters by wavefield extrapo-
699 lation. *Geophysical Journal International*, *71*(3), 613–628.
- 700 McMechan, G. A. (1983). Migration by extrapolation of time-dependent boundary
701 values. *Geophysical prospecting*, *31*(3), 413–420.
- 702 Meltzer, A., Rudnick, R., Zeitler, P., Levander, A., Humphreys, G., Karlstrom, K.,

- 703 ... others (1999). The USArray initiative. *Geological Society of America*
704 *Today*, 9, 8–10.
- 705 Millet, F., Bodin, T., & Rondenay, S. (2019). Multimode 3-D Kirchhoff migration of
706 receiver functions at continental scale. *Journal of Geophysical Research: Solid*
707 *Earth*, 124(8), 8953–8980.
- 708 Mora, P. (1989). Inversion= migration+ tomography. *Geophysics*, 54(12), 1575–
709 1586.
- 710 Morozova, E., Wan, X., Chamberlain, K. R., Smithson, S. B., Morozov, I. B., Boyd,
711 N. K., ... Foster, C. (2002). Geometry of Proterozoic sutures in the central
712 Rocky Mountains from seismic reflection data: Cheyenne belt and Farwell
713 Mountain structures. *Geophysical Research Letters*, 29(13), 17–1.
- 714 Nábělek, J., Hetényi, G., Vergne, J., Sapkota, S., Kafle, B., Jiang, M., ... Team,
715 t. H.-C. (2009). Underplating in the Himalaya-Tibet collision zone revealed by
716 the Hi-CLIMB experiment. *Science*, 325(5946), 1371–1374.
- 717 Nakata, N., & Beroza, G. C. (2016). Reverse time migration for microseismic sources
718 using the geometric mean as an imaging condition. *Geophysics*, 81(2), KS51–
719 KS60.
- 720 Notfors, C., Xie, Y., & Gray, S. (n.d.). Gaussian Beam Migration-A Viable Alter-
721 native to Kirchhoff? In *68th EAGE Conference and Exhibition incorporating*
722 *SPE EUROPEC 2006*, pages=cp-2, year=2006, organization=EAGE Publica-
723 tions BV.
- 724 Okada, Y., Kasahara, K., Hori, S., Obara, K., Sekiguchi, S., Fujiwara, H., & Ya-
725 mamoto, A. (2004). Recent progress of seismic observation networks in
726 Japan—Hi-net, F-net, K-NET and KiK-net. *Earth, Planets and Space*, 56(8),
727 xv–xxviii.
- 728 Onyango, E. A., Worthington, L. L., Schmandt, B., & Abers, G. A. (2022). Subduc-
729 tion Zone Interface Structure within the Southern MW9. 2 1964 Great Alaska
730 Earthquake Asperity: Constraints from Receiver Functions Across a Spatially
731 Dense Node Array. *Geophysical Research Letters*, 49(15), e2022GL098334.
- 732 Owens, T. J., Crotwell, H. P., Groves, C., & Oliver-Paul, P. (2004). SOD: Standing
733 order for data. *Seismological Research Letters*, 75(4), 515–520.
- 734 Prodehl, C., Lipman, P. W., Pakiser, L., & Mooney, W. (1989). Crustal structure of
735 the Rocky Mountain region. *Geophysical framework of the continental United*

- 736 States, 172, 249–284.

737 Rajasekaran, S., & McMechan, G. A. (1995). Prestack processing of land data with
738 complex topography. *Geophysics*, 60(6), 1875–1886.

739 Richards, P. G., & Aki, K. (1980). *Quantitative seismology: theory and methods*
740 (Vol. 859). Freeman San Francisco, CA.

741 Rondenay, S. (2009). Upper mantle imaging with array recordings of converted and
742 scattered teleseismic waves. *Surveys in geophysics*, 30, 377–405.

743 Rondenay, S., Bostock, M. G., Hearn, T. M., White, D. J., & Ellis, R. M. (2000).
744 Lithospheric assembly and modification of the SE Canadian Shield: Abitibi-
745 Grenville teleseismic experiment. *Journal of Geophysical Research: Solid
746 Earth*, 105(B6), 13735–13754.

747 Ruigrok, E., Campman, X., Draganov, D., & Wapenaar, K. (2010). High-resolution
748 lithospheric imaging with seismic interferometry. *Geophysical Journal Interna-*
749 *tional*, 183(1), 339–357.

750 Schäfer, M., Groos, L., Forbriger, T., & Bohlen, T. (2014). Line-source simulation
751 for shallow-seismic data. Part 2: Full-waveform inversion—A synthetic 2-D
752 case study. *Geophysical Journal International*, 198(3), 1405–1418.

753 Schneider, W. A. (1978). Integral formulation for migration in two and three dimen-
754 sions. *Geophysics*, 43(1), 49–76.

755 Shang, X., de Hoop, M. V., & van der Hilst, R. D. (2012). Beyond receiver func-
756 tions: Passive source reverse time migration and inverse scattering of converted
757 waves. *Geophysical Research Letters*, 39(15).

758 Shang, X., de Hoop, M. V., & van der Hilst, R. D. (2017). Common conversion
759 point stacking of receiver functions versus passive-source reverse time migra-
760 tion and wavefield regularization. *Geophysical Journal International*, 209(2),
761 923–934.

762 Sheehan, A. F., Shearer, P. M., Gilbert, H. J., & Dueker, K. G. (2000). Seismic mi-
763 gration processing of P-SV converted phases for mantle discontinuity structure
764 beneath the Snake River Plain, western United States. *Journal of Geophysical
765 Research: Solid Earth*, 105(B8), 19055–19065.

766 Shen, W., & Ritzwoller, M. H. (2016). Crustal and uppermost mantle structure
767 beneath the United States. *Journal of Geophysical Research: Solid Earth*,
768 121(6), 4306–4342.

- 769 Shepard, D. (n.d.). A two-dimensional interpolation function for irregularly-spaced
770 data. In *Proceedings of the 1968 23rd ACM national conference, pages=517–524, year=1968.*
- 772 Shragge, J. (2014). Reverse time migration from topography. *Geophysics*, 79(4),
773 S141–S152.
- 774 Sims, P. K., & Stein, H. J. (2003). Tectonic evolution of the Proterozoic Colorado
775 province, Southern Rocky Mountains: A summary and appraisal. *Rocky Mountain
776 Geology*, 38(2), 183–204.
- 777 Snelson, C. M., Henstock, T. J., Keller, G. R., Miller, K. C., & Levander, A. (1998).
778 Crustal and uppermost mantle structure along the Deep Probe seismic profile.
779 *Rocky Mountain Geology*, 33(2), 181–198.
- 780 Spitz, S. (1991). Seismic trace interpolation in the FX domain. *Geophysics*, 56(6),
781 785–794.
- 782 Sun, R., McMechan, G. A., Hsiao, H.-H., & Chow, J. (2004). Separating P-and
783 S-waves in prestack 3D elastic seismograms using divergence and curl. *Geo-
784 physics*, 69(1), 286–297.
- 785 Tape, C., Liu, Q., Maggi, A., & Tromp, J. (2009). Adjoint tomography of the south-
786 ern California crust. *Science*, 325(5943), 988–992.
- 787 Tong, P. (2021). Adjoint-state travelttime tomography: Eikonal equation-based meth-
788 ods and application to the Anza Area in Southern California. *Journal of Geo-
789 physical Research: Solid Earth*, 126(5), e2021JB021818.
- 790 Tong, P., Chen, C.-w., Komatitsch, D., Basini, P., & Liu, Q. (2014). High-resolution
791 seismic array imaging based on an SEM-FK hybrid method. *Geophysical Journal
792 International*, 197(1), 369–395.
- 793 Tong, P., Komatitsch, D., Tseng, T.-L., Hung, S.-H., Chen, C.-W., Basini, P., &
794 Liu, Q. (2014). A 3-D spectral-element and frequency-wave number hybrid
795 method for high-resolution seismic array imaging. *Geophysical Research Let-
796 ters*, 41(20), 7025–7034.
- 797 Trad, D. (2009). Five-dimensional interpolation: Recovering from acquisition con-
798 straints. *Geophysics*, 74(6), V123–V132.
- 799 Tromp, J. (2020). Seismic wavefield imaging of Earth’s interior across scales. *Nature
800 Reviews Earth & Environment*, 1(1), 40–53.
- 801 Tromp, J., Tape, C., & Liu, Q. (2005). Seismic tomography, adjoint methods, time

- reversal and banana-doughnut kernels. *Geophysical Journal International*, *160*(1), 195–216.
- Tyson, A. R., Morozova, E., Karlstrom, K., Dueker, K. C. S. S. K., & Foster, C. (2002). Proterozoic Farwell Mountain–Lester Mountain suture zone, northern Colorado: Subduction flip and progressive assembly of arcs. *Geology*, *30*(10), 943–946.
- VanDecar, J., & Crosson, R. (1990). Determination of teleseismic relative phase arrival times using multi-channel cross-correlation and least squares. *Bulletin of the Seismological Society of America*, *80*(1), 150–169.
- Vinnik, L. (1977). Detection of waves converted from P to SV in the mantle. *Physics of the Earth and planetary interiors*, *15*(1), 39–45.
- Waheed, U. B., Yarman, C. E., & Flagg, G. (2015). An iterative, fast-sweeping-based eikonal solver for 3D tilted anisotropic media. *Geophysics*, *80*(3), C49–C58.
- Wang, K., Jiang, C., Yang, Y., Schulte-Pelkum, V., & Liu, Q. (2020). Crustal deformation in southern California constrained by radial anisotropy from ambient noise adjoint tomography. *Geophysical Research Letters*, *47*(12), e2020GL088580.
- Wang, K., Yang, Y., Jiang, C., Wang, Y., Tong, P., Liu, T., & Liu, Q. (2021). Adjoint tomography of ambient noise data and teleseismic P waves: Methodology and applications to central California. *Journal of Geophysical Research: Solid Earth*, *126*(6), e2021JB021648.
- Wang, X., Zhan, Z., Zhong, M., Persaud, P., & Clayton, R. W. (2021). Urban basin structure imaging based on dense arrays and bayesian array-based coherent receiver functions. *Journal of Geophysical Research: Solid Earth*, *126*(9), e2021JB022279.
- Wang, Y., Chevrot, S., Monteiller, V., Komatitsch, D., Mouthereau, F., Manatschal, G., ... others (2016). The deep roots of the western Pyrenees revealed by full waveform inversion of teleseismic P waves. *Geology*, *44*(6), 475–478.
- Wessel, P., Luis, J., Uieda, L., Scharroo, R., Wobbe, F., Smith, W. H., & Tian, D. (2019). The generic mapping tools version 6. *Geochemistry, Geophysics, Geosystems*, *20*(11), 5556–5564.
- Whitmore, N. D. (1983). Iterative depth migration by backward time propagation.

- 835 In *Seg technical program expanded abstracts 1983* (pp. 382–385). Society of Ex-
836 ploration Geophysicists.
- 837 Wilson, D., & Aster, R. (2005). Seismic imaging of the crust and upper mantle
838 using regularized joint receiver functions, frequency–wave number filtering, and
839 multimode Kirchhoff migration. *Journal of Geophysical Research: Solid Earth*,
840 110(B5).
- 841 Withers, M., Aster, R., Young, C., Beiriger, J., Harris, M., Moore, S., & Trujillo, J.
842 (1998). A comparison of select trigger algorithms for automated global seismic
843 phase and event detection. *Bulletin of the Seismological Society of America*,
844 88(1), 95–106.
- 845 Wu, S.-M., Huang, H.-H., Lin, F.-C., Farrell, J., & Schmandt, B. (2023). Extreme
846 seismic anisotropy indicates shallow accumulation of magmatic sills beneath
847 Yellowstone caldera. *Earth and Planetary Science Letters*, 616, 118244.
- 848 Xu, S., Zhang, Y., Pham, D., & Lambaré, G. (2005). Antileakage Fourier transform
849 for seismic data regularization. *Geophysics*, 70(4), V87–V95.
- 850 Yang, J., Huang, J., Zhu, H., McMechan, G., & Li, Z. (2022). Introduction to a
851 Two-Way Beam Wave Method and Its Applications in Seismic Imaging. *Jour-*
852 *nal of Geophysical Research: Solid Earth*, 127(6), e2021JB023357.
- 853 Yang, J., Zhu, H., & Lumley, D. (2020). Time-lapse imaging of coseismic ruptures
854 for the 2019 ridgecrest earthquakes using multiazimuth backprojection with
855 regional seismic data and a 3-D crustal velocity model. *Geophysical Research*
856 *Letters*, 47(9), e2020GL087181.
- 857 Yang, J., Zhu, H., Wang, W., Zhao, Y., & Zhang, H. (2018). Isotropic elastic re-
858 verse time migration using the phase-and amplitude-corrected vector P-and
859 S-wavefields. *Geophysics*, 83(6), S489–S503.
- 860 Yang, X., Pavlis, G. L., Hamburger, M. W., Marshak, S., Gilbert, H., Rupp, J., ...
861 Carpenter, N. S. (2017). Detailed crustal thickness variations beneath the Illi-
862 nois Basin area: Implications for crustal evolution of the midcontinent. *Journal*
863 *of Geophysical Research: Solid Earth*, 122(8), 6323–6345.
- 864 Yi, J., Liu, Y., Yang, Z., Lu, H., He, B., & Zhang, Z. (2019). A least-squares
865 correlation-based full travelttime inversion for shallow subsurface velocity recon-
866 struction. *Geophysics*, 84(4), R613–R624.
- 867 Yuan, X., Kind, R., Li, X., & Wang, R. (2006). The S receiver functions: synthetics

- and data example. *Geophysical Journal International*, 165(2), 555–564.
- Zhang, C., Yao, H., Liu, Q., Zhang, P., Yuan, Y. O., Feng, J., & Fang, L. (2018). Linear array ambient noise adjoint tomography reveals intense crust-mantle interactions in North China Craton. *Journal of Geophysical Research: Solid Earth*, 123(1), 368–383.
- Zhang, H., van der Lee, S., Wolin, E., Bollmann, T. A., Revenaugh, J., Wiens, D. A., ... others (2016). Distinct crustal structure of the North American Midcontinent Rift from P wave receiver functions. *Journal of Geophysical Research: Solid Earth*, 121(11), 8136–8153.
- Zhang, J., & Zheng, T. (2015). Receiver function imaging with reconstructed wavefields from sparsely scattered stations. *Seismological Research Letters*, 86(1), 165–172.
- Zhao, D., Hasegawa, A., & Horiuchi, S. (1992). Tomographic imaging of P and S wave velocity structure beneath northeastern Japan. *Journal of Geophysical Research: Solid Earth*, 97(B13), 19909–19928.
- Zhao, H. (2005). A fast sweeping method for eikonal equations. *Mathematics of computation*, 74(250), 603–627.
- Zheng, T., Zhao, L., & Zhu, R. (2008). Insight into the geodynamics of cratonic reactivation from seismic analysis of the crust-mantle boundary. *Geophysical Research Letters*, 35(8).
- Zhu, H. (2017). Elastic wavefield separation based on the Helmholtz decompositionElastic wavefield separation. *Geophysics*, 82(2), S173–S183.
- Zhu, H., Bozdağ, E., Peter, D., & Tromp, J. (2012). Structure of the European upper mantle revealed by adjoint tomography. *Nature Geoscience*, 5(7), 493–498.
- Zhu, H., Stern, R. J., & Yang, J. (2020). Seismic evidence for subduction-induced mantle flows underneath Middle America. *Nature communications*, 11(1), 2075.
- Zhu, L. (2000). Crustal structure across the San Andreas Fault, southern California from teleseismic converted waves. *Earth and Planetary Science Letters*, 179(1), 183–190.

Table 1: Teleseismic event information for passive source RTM using the Laramie array.

Event	Original Time	Lon(°)	Lat(°)	Depth(km)
P1	2000_10_04_14_37_44	-62.5590	11.1240	110.3
P2	2000_10_05_13_39_11	-40.9580	31.7320	10
P3	2000_11_08_06_59_58	-77.8290	7.0420	17
P4	2000_11_29_10_25_13	-70.8860	-24.8690	58.2
P5	2000_12_12_05_26_45	-82.6790	6.0150	10
P6	2001_01_10_16_02_42	-153.2810	56.7744	36.4
P7	2001_01_13_17_33_32	-88.6600	13.0490	60
P8	2001_02_13_14_22_05	-88.9380	13.6710	10
P9	2001_03_24_06_27_53	132.5260	34.0830	50
P10	2001_04_09_09_00_57	-73.1090	-32.6680	11
P11	2001_04_14_23_27_26	141.7680	30.0920	10
S1	2000_10_04_16_58_44	166.9100	-15.4210	23
S2	2000_10_27_04_21_51	140.4600	26.2660	388
S3	2000_10_29_08_37_08	153.9450	-4.7660	50
S4	2000_12_21_01_01_27	151.1220	-5.7060	33
S5	2001_01_09_16_49_28	167.1700	-14.9280	103
S6	2001_04_09_09_00_57	-73.1090	-32.6680	11
S7	2001_04_14_23_27_26	141.7680	30.0920	10
S8	2001_04_28_04_49_53	-176.9370	-18.0640	351.8

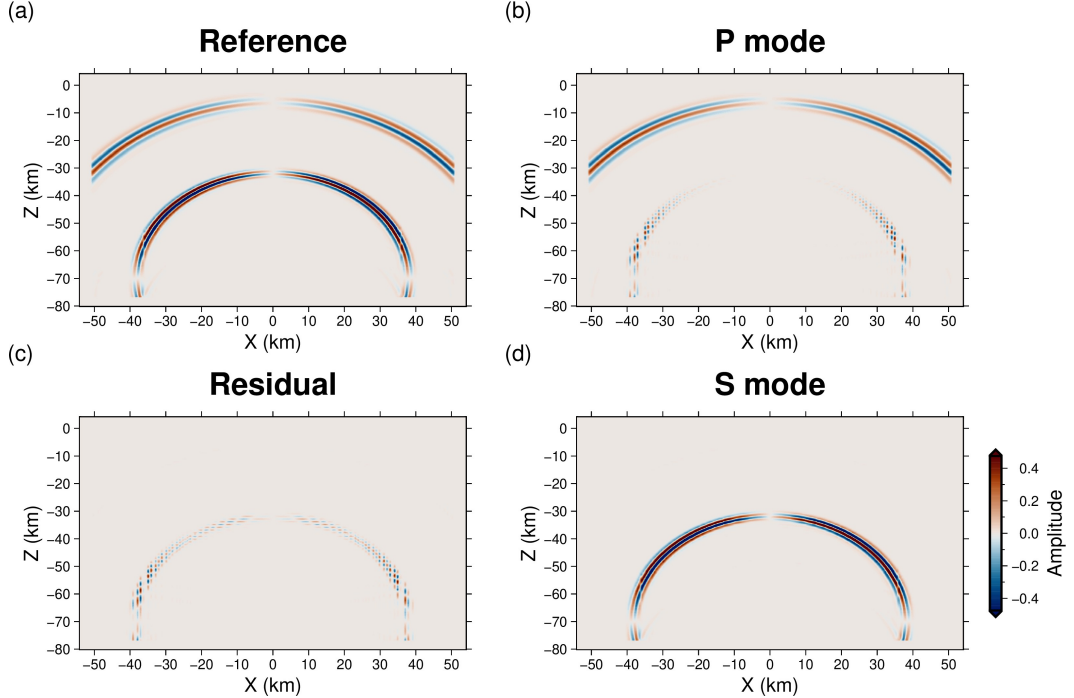


Figure 1: Strong-form solutions for wavefield decomposition based on Equation 6. Panel (a) shows the X component of the back-propagating elastic wavefield. Panels (b) and (d) represent the separated P and S wavefields, respectively. Panel (c) shows the difference between the reference (a) and the summation of strong-form decomposed P (b) and S (d) waves. The Z component has a similar phenomenon, which is not shown here.

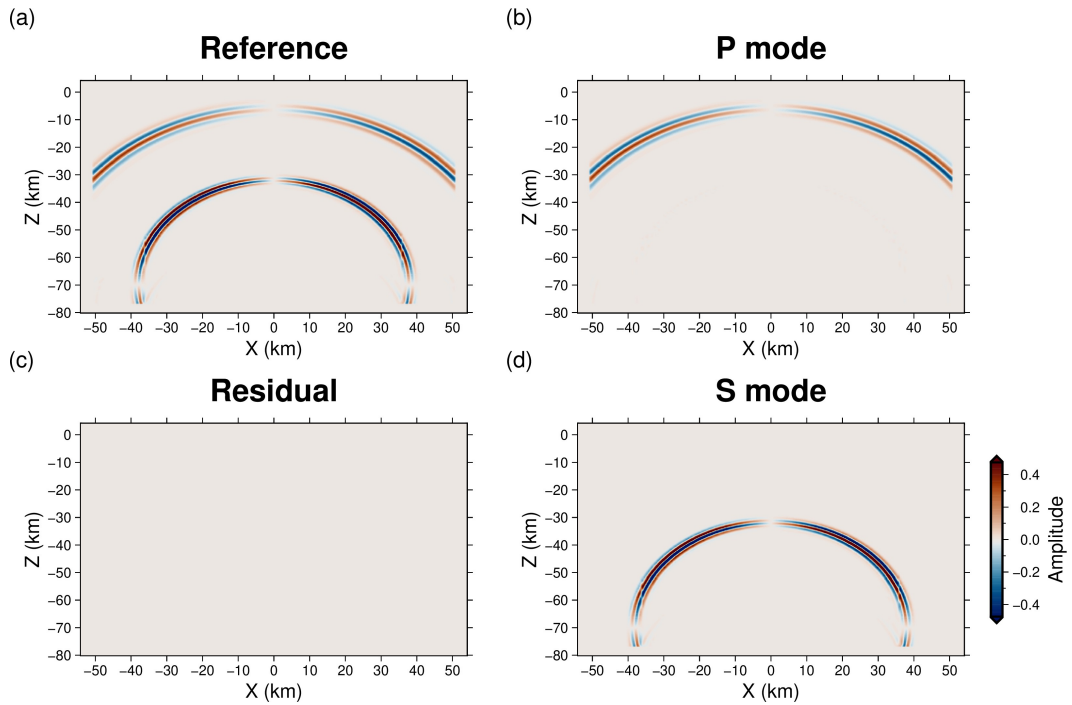


Figure 2: Same as Figure 1 but shows the decomposed wavefields based on Equations 7 and 8.

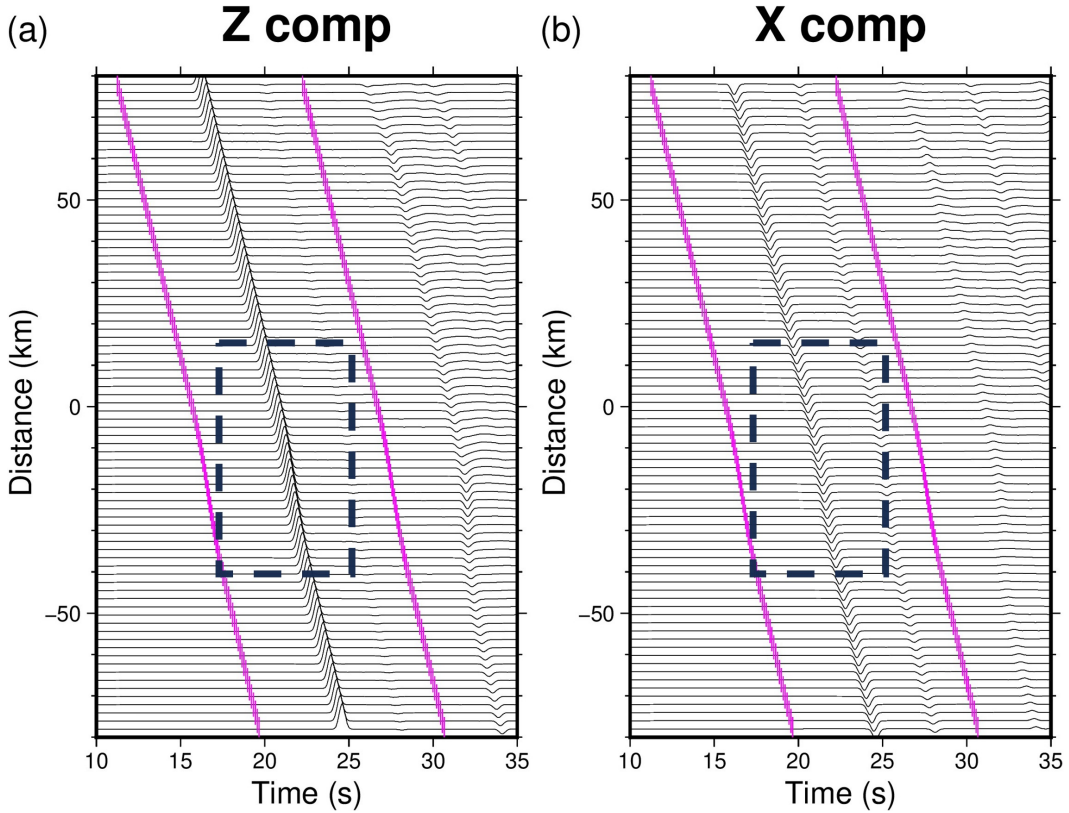


Figure 3: Synthetic teleseismic data with topographic changes in the model shown in Figure 4b. Panels (a) and (b) are Z and X component seismograms, respectively. The plane wave incident depth is 120 km, with a back azimuthal angle of 90° , and an incident angle of 27° . Therefore, X components could be considered as the radial components of teleseismic waves. The black dashed rectangle highlights the effect of topographic changes on recorded data. The magenta short lines denote the time window used to isolate waveforms for RTM.

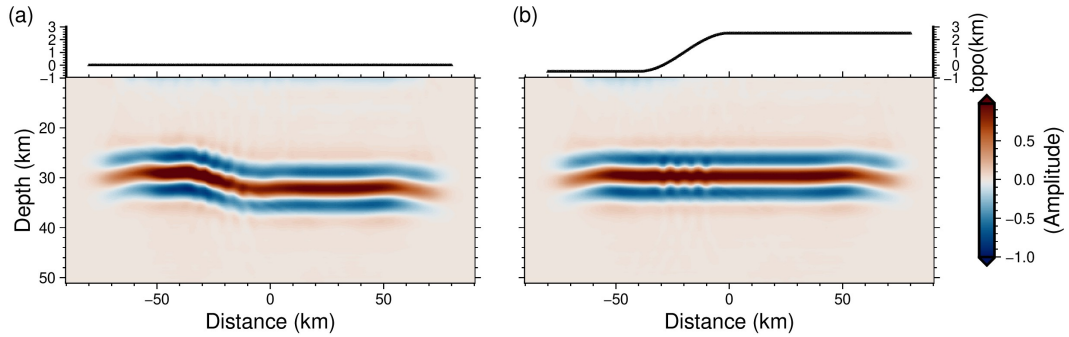


Figure 4: passive source RTM using 12 teleseismic events with incident-angles ranging from 12° to 27° . The back-azimuthal angle for the first six events is 90° and is 270° for the others. The black line on top of the image represents the station locations for injecting adjoint sources during migration. (a) Without considering the topographic variation, i.e., the stations are assumed to be at 0 km depth. (b) By considering the topographic variations, the stations are modeled at the correct elevations.

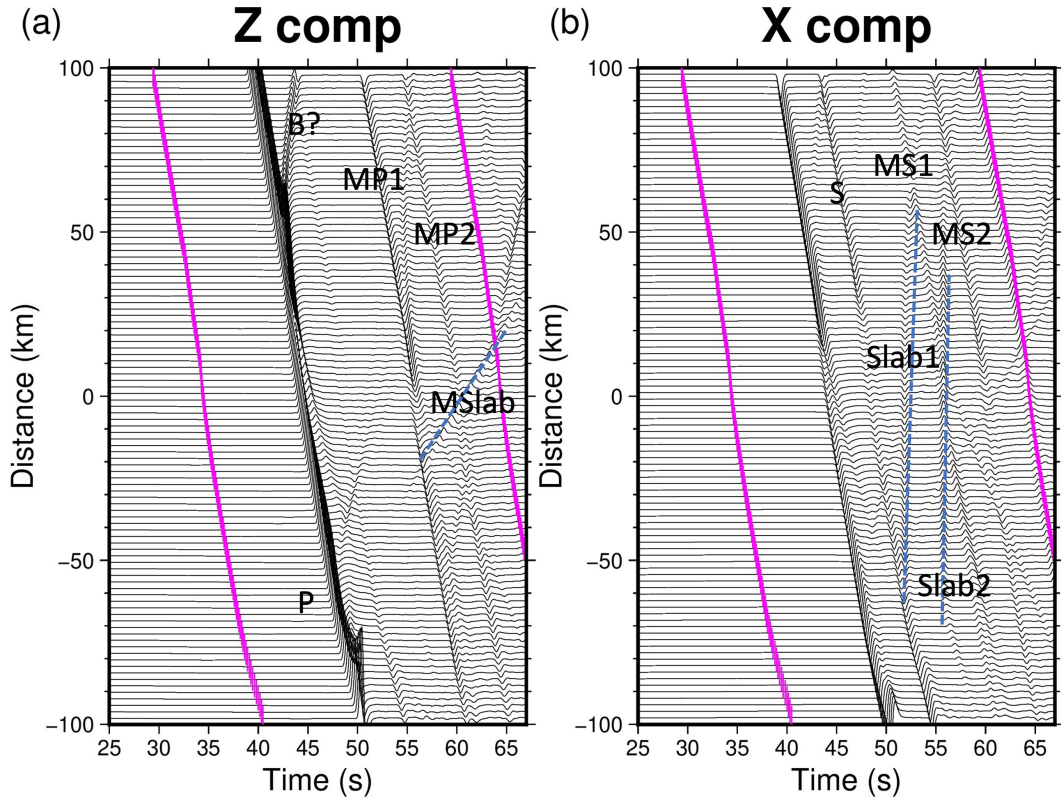


Figure 5: Synthetic Z (a) and X (b) components for the first teleseismic event with an incident angle of 27° and a back azimuthal angle of 90° . The magenta short lines denote the time window used to isolate waveforms for RTM. In panel (a), P denotes teleseismic P waves, MP1 and MP2 represent different-order P wave multiples. MSlab together with the dashed blue line, represent slab-related multiples. B is used to denote reflection artifacts due to absorbing boundary conditions. In panel (b), S denotes Ps-converted waves, MS1 and MS2 are corresponding P-multiple converted waves. Slab1 and Slab2 are slab-related Ps-converted waves.

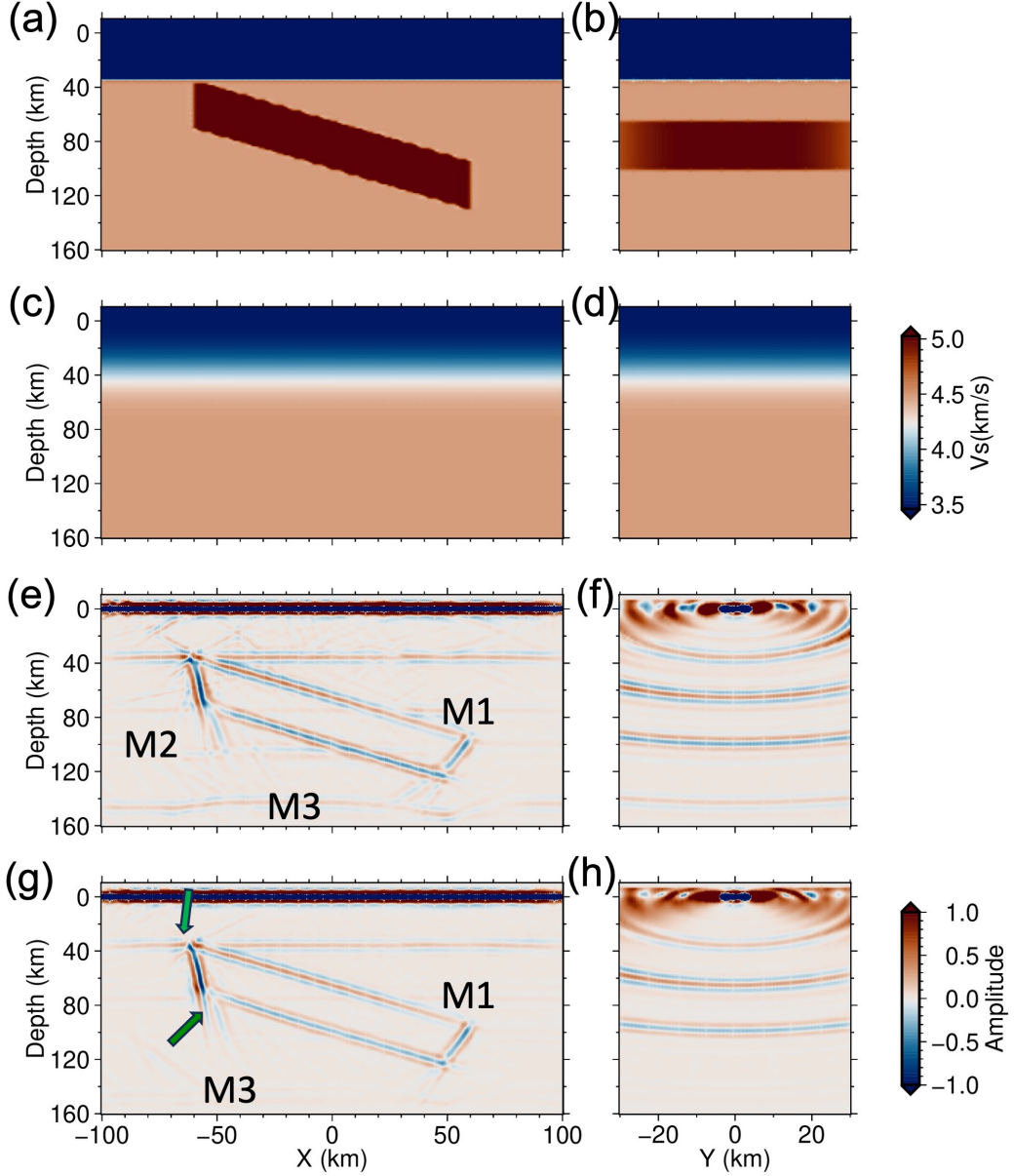


Figure 6: 3-D subducting slab imaging using 12 teleseismic events. The incident angle of the incident wavefield ranges from 12° to 27° . The back-azimuthal angle for events 1, 3, 7, 9 and 11 is 90° and 270° for the others. Panels (a) and (b) show the true velocity profile along the X (west-east) and Y (north-source) directions for generating synthetic datasets. Panels (c) and (d) show the corresponding migration velocity along the same profiles, which is smoothed from the two-layer background model after removing the slab. Panels (e) and (f) show the stacked images from the first four teleseismic events, while panels (g) and (h) show the final image stacked over all teleseismic events. Panels (e-h) share the same color bars. M1, M2 and M3 in panels (e) and (g) represent multiple artifacts. The artifacts pointed by the green arrows are caused by strong scattering at the sharp edges of the slab.

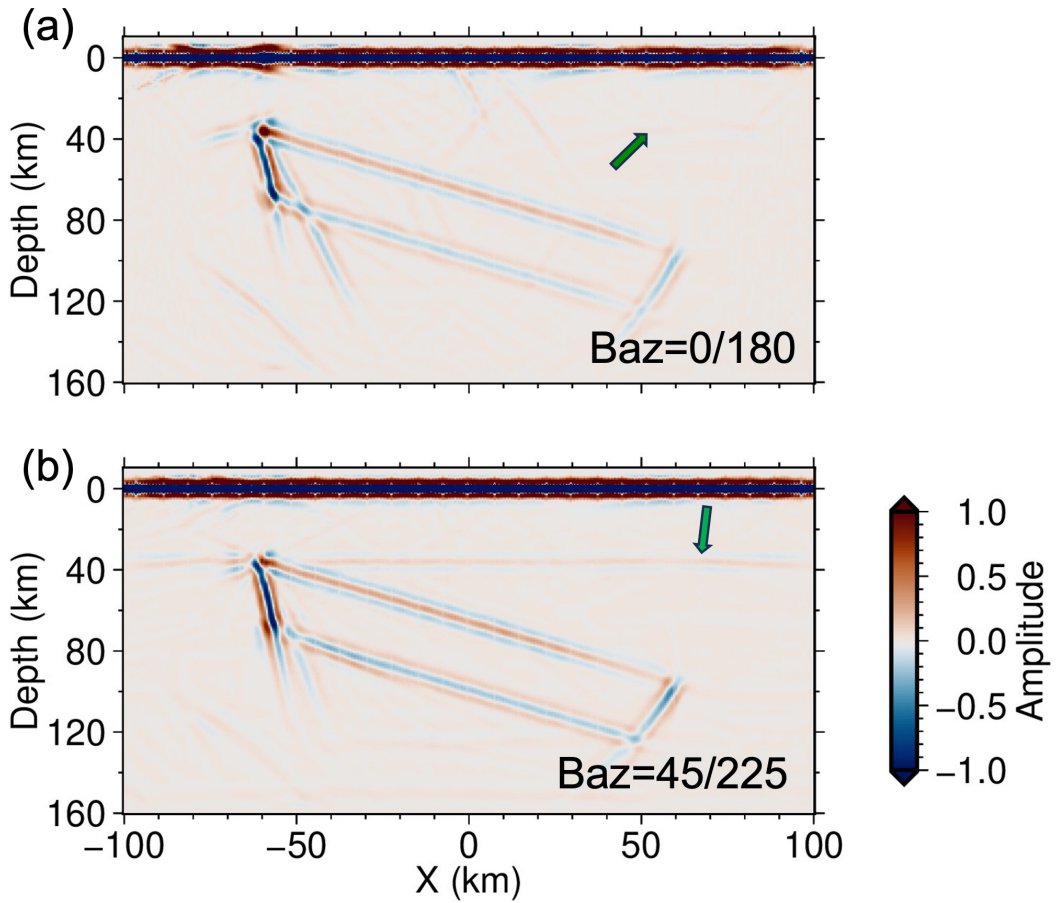


Figure 7: Similar to panel (g) in Figure 6, but the back azimuthal angles used for these two examples are 0° for events 1, 3, 7, 9 and 11, and 180° for the others (a), which are 45° and 225° in panel (b). The green arrows are used to compare imaged Moho interfaces with Figure 6.

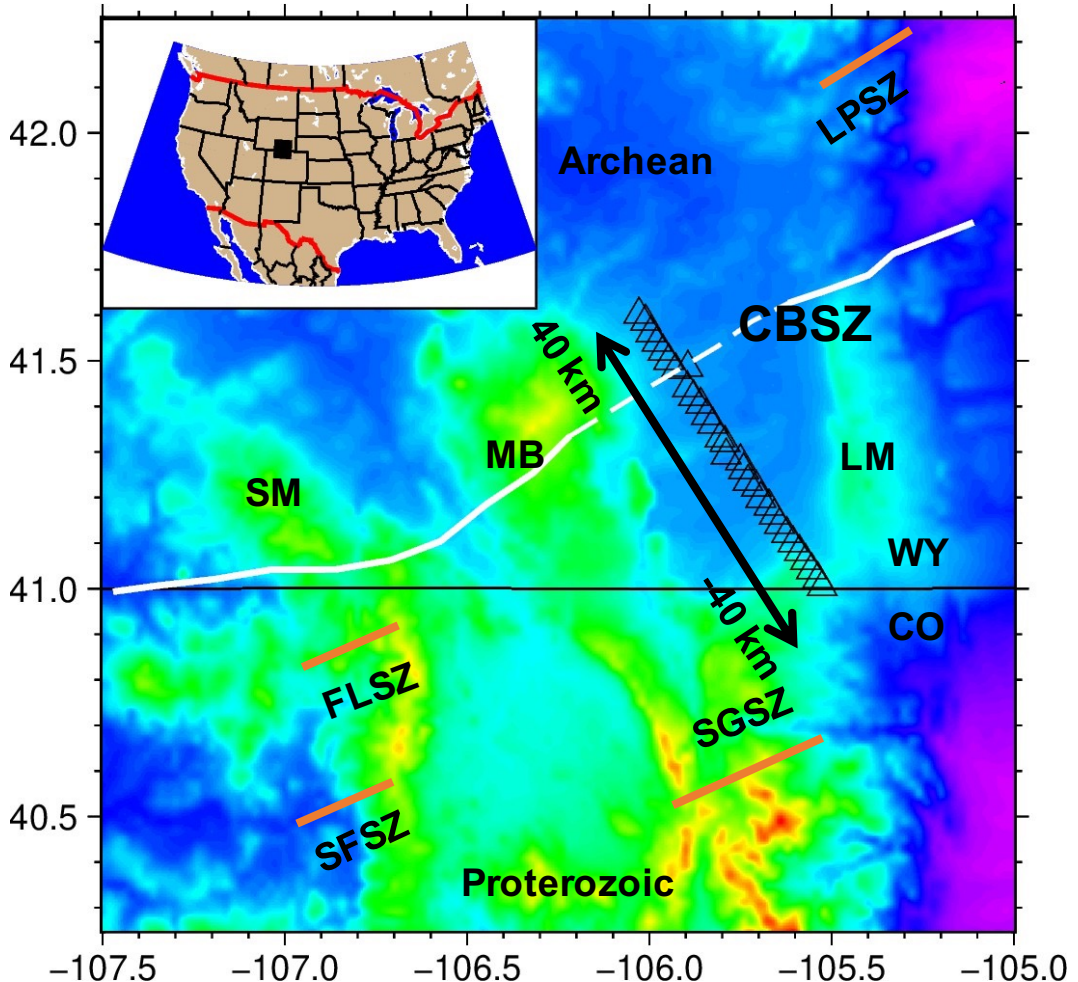


Figure 8: Geological settings of the study region after Hansen and Dueker (2009). The background shows the topography. Several shear zones: LPSZ, Laramie Peak shear zone; FLSZ, Farwell Mt. Lester Mt. suture zone; SFSZ, Soda Creek-Fish Creek shear zone; SGSZ, Skin Gulch shear zone, are denoted by orange lines to illustrate the complexity of the subsurface structures. Other geographic features: SM, Sierra Madres; MB, Medicine Bow Mountains and LM, Laramie Mountains are also labeled. The Cheyenne Belt suture (CB) is denoted by the white line, dashed where it is inferred. WY and CO denotes Wyoming and Colorado, respectively. The black rectangle in the upper-left inset map indicates the location of our study region in North America.

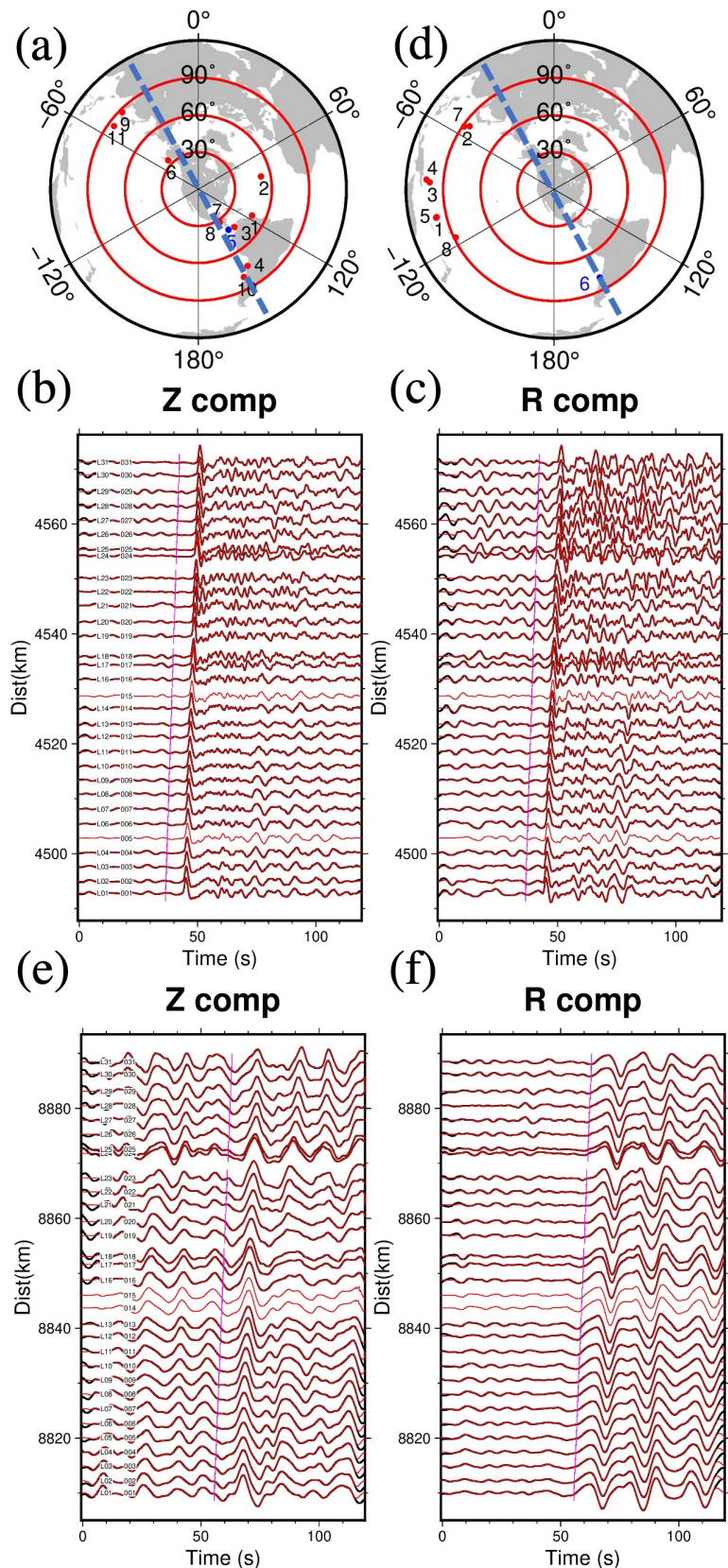


Figure 9: Caption next page.

Figure 9: Telseismic events and data used for migration. Red dots in Panels (a) and (d) represent the distributions of teleseismic P and S events. The light blue dashed line indicates the direction of the Laramie array. Panels (b) and (c) show the vertical (Z) and radial (R) components of the 5th (the blue dot in panel a) teleseismic P events recorded by the Laramie array. The background black solid lines denote the selected high-quality data (some traces are removed due to low signal-to-noise ratio), while the red solid lines represent the 2-D cubic-spline interpolated data at each station. Panels (e) and (f) represent the vertical and radial components of the 6th teleseismic S events. The magenta lines overlaying the seismograms denote either the onsets of P or S waves.

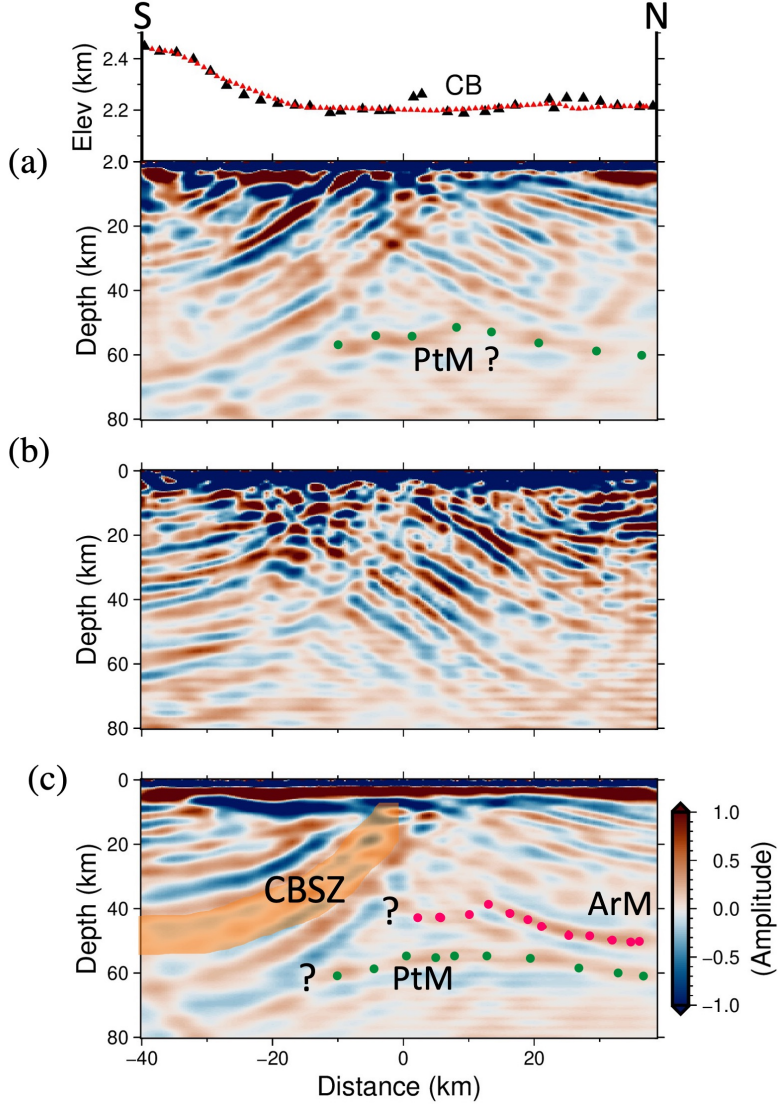


Figure 10: The passive source RTM image beneath the Laramie array. On the top of the figure, we show the elevation of raw (black triangles) and interpolated (red triangles) stations. CB represents the inferred CBSZ location on the surface. Panels (a) and (b) show the images obtained using teleseismic P and S events, respectively. Panel (c) shows the image obtained using interpolated telesismic P events. The orange belt indicates the interpreted CBSZ. The magenta and dark green dots indicate the interpreted Archean Moho (ArM) and Proterozoic Moho (PtM).

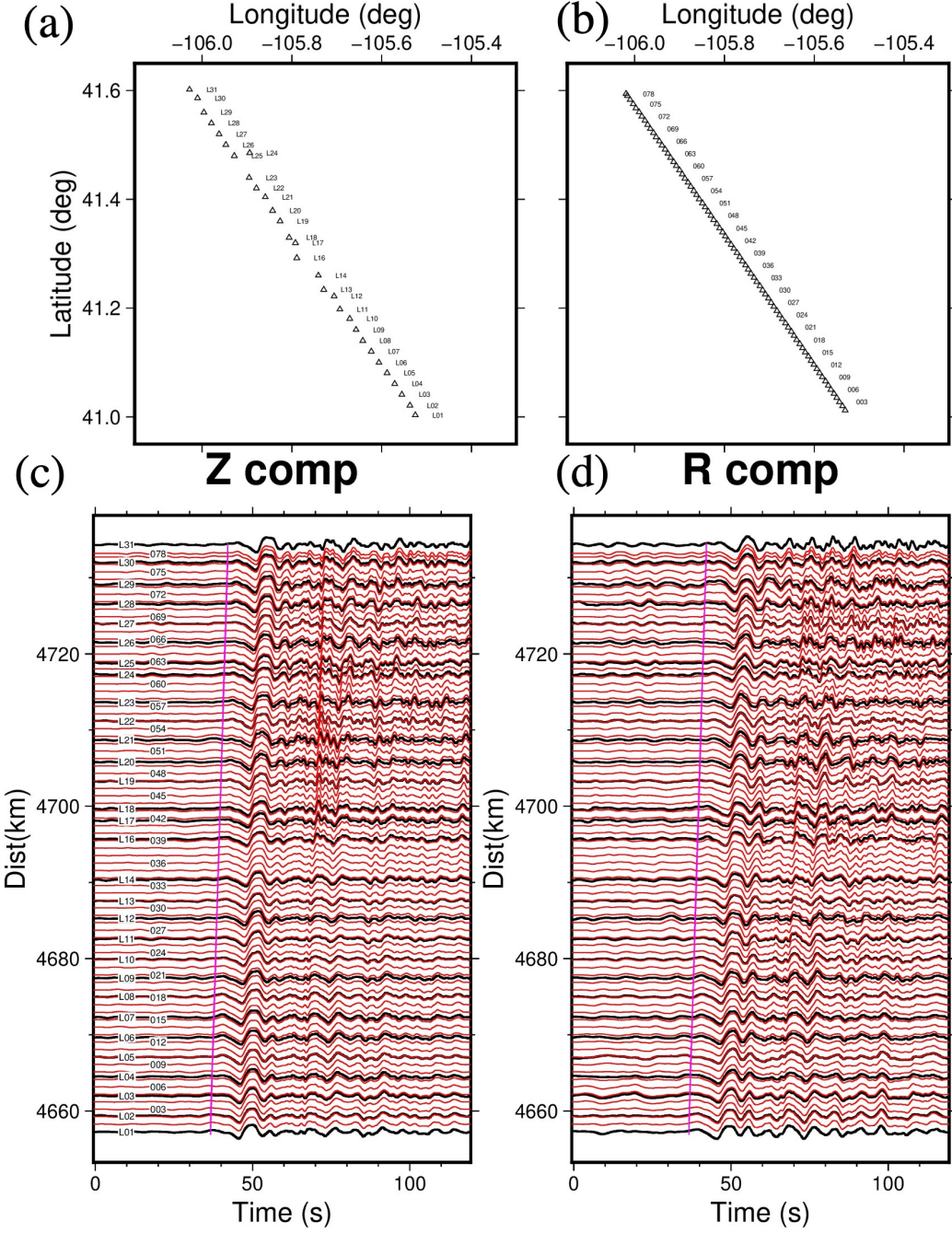


Figure 11: Regularization of the recorded teleseismic data to a fine grid. Panels (a) and (b) compare the raw and interpolation station locations. The interpolated station locations are obtained with GMT projection between the first (L01) and last station (L31) positions of the Laramie array along the great circle for every 1.0 km, which is not on a straight line after the UTM projection. Panels (c) and (d) show comparisons of the raw data (black) and interpolated seismograms (red) for vertical (Z) and radial (R) components, respectively.

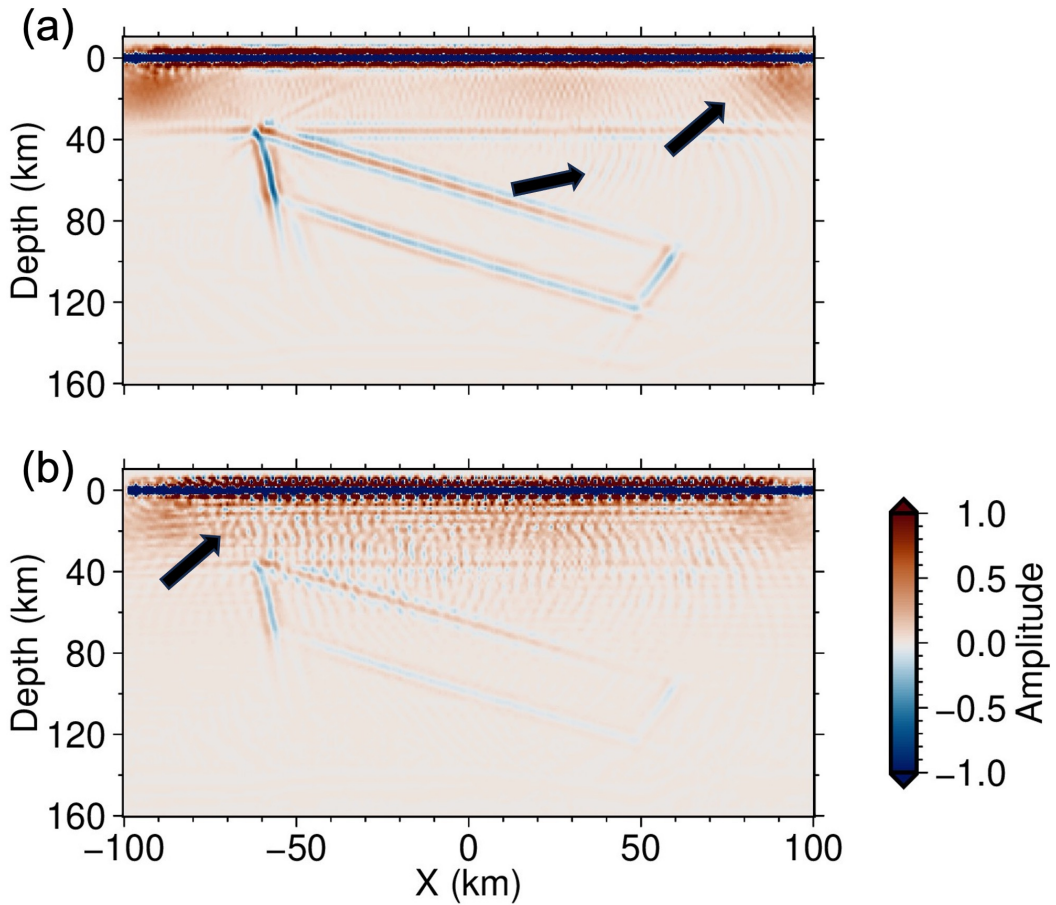


Figure 12: Imaging with sparse station spacing. The imaging parameters are the same as panel (g) in Figure 6 except that the station spacing is 2 km and 4 km for panels (a) and (b), respectively. The aliasing artifacts are illustrated by black arrows.

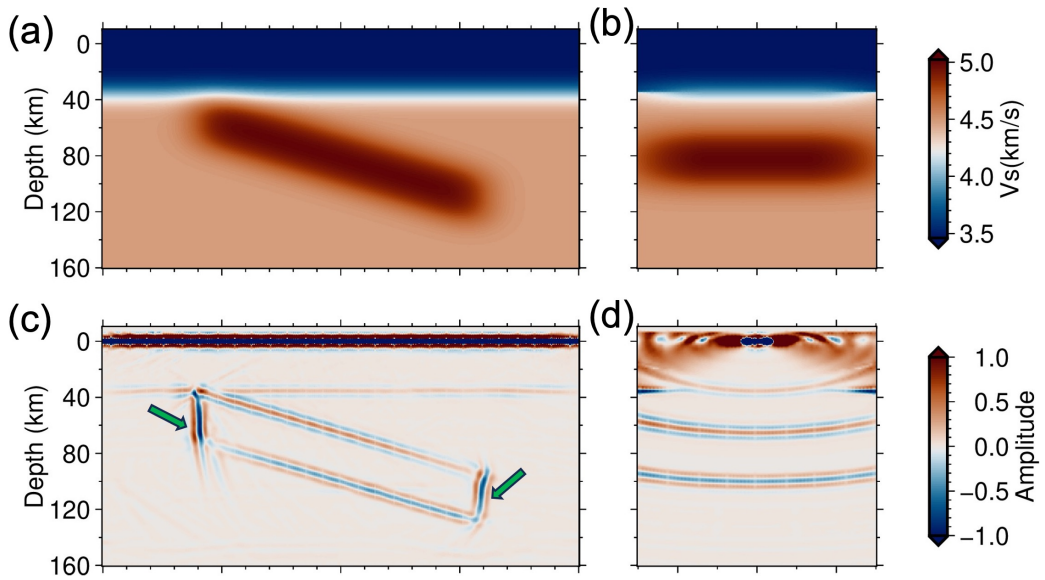


Figure 13: Imaging with a more accurate background migration velocity model. Panels (a) and (b) show the migration velocity profiles along the X (west-east) and Y (north-source) directions. Panels (c) and (d) show the corresponding RTM images. The green arrows are used to highlight the improvement in imaging of the slab boundaries compared to panel (g) in Figure 6.